https://doi.org/10.5194/egusphere-2025-967
Preprint. Discussion started: 17 March 2025

Life cycle studies and liquid-phase characterization of Arctic mixed-phase clouds: MOSAiC 2019-2020 results

Cristofer Jimenez[1], Albert Ansmann[1], Kevin Ohneiser[1], Hannes Griesche[1], Ronny Engelmann[1], Martin Radenz[1], Julian Hofer[1], Dietrich Althausen[1], Daniel A. Knopf[2], Sandro Dahlke[3], Johannes Bühl[1,4], Holger Baars[1], Patric Seifert[1], and Ulla Wandinger[1]

[1]Leibniz Institute for Tropospheric Research, Leipzig, Germany
[2]School of Marine and Atmospheric Sciences, Stony Brook University, Stony Brook, NY 11794, USA
[3]Alfred Wegener Institute, Helmholtz Centre for Polar and Marine Research, Potsdam, Germany
[4]Harz University of Applied Sciences, Wernigerode, Germany

Correspondence: C. Jimenez
(jimenez@tropos.de)

Abstract.

Height-resolved monitoring of life cycles of mixed-phase clouds (MPCs) was performed in the free troposphere over the central Arctic during the MOSAiC (Multidisciplinary drifting Observatory for the Study of Arctic Climate) expedition from October 2019 to September 2020. The research icebreaker *Polarstern*, drifting with the pack ice for more than seven months, served as a platform for state-of-the-art remote sensing of aerosols and clouds. The use of the recently introduced dual field-of-view (FOV) polarization lidar technique in combination with the well-established lidar-radar retrieval technique provided, for the first time, a robust instrumental basis to monitor the evolution of the liquid and the ice phase of MPCs and the interplay between the two phases. We discuss two long-lasting Arctic MPC cases (one mid winter case and one late summer case) observed close to the North Pole in December 2019 and in September 2020. During the late summer MPC event, most likely three gravity waves strongly disturbed the cloud evolution. We documented this perturbation in detail in terms of liquid and ice phase properties and the recovery of the strongly disturbed liquid phase within a few hours. For the first time, cloud statistics, covering all seasons of a year, are presented for liquid-bearing stratiform clouds in the central Arctic. The focus is on the optical and microphysical properties of the liquid phase which is of key importance for a long MPC lifetime. The MOSAiC observations confirmed that ice formation occurs predominantly via immersion freezing (with mineral dust as main ice nucleation particle type). We also found that activation of aerosol particles to form water droplets is of great importance for the longevity of MPCs and that the free tropospheric reservoirs of cloud condensation nuclei and ice-nucleating particles seem to be usually well filled.

1 Introduction

Stratiform mixed-phase clouds (MPCs) occur everywhere around the globe from the tropics to the poles, at all altitudes with temperatures from 0° down to −36°C. Arctic MPCs exert a sensitive impact on the radiation field and temperature conditions in the polar regions as well as on the evolution of precipitation and thus on the vertical exchange of water in the polar troposphere

https://doi.org/10.5194/egusphere-2025-967
Preprint. Discussion started: 17 March 2025

(Lohmann and Neubauer, 2018; Wendisch et al., 2019; Morrison et al., 2020). Therefore, a careful consideration of MPCs in climate and weather prediction models is a clear need. However, because these clouds show complex microphysical and thermodynamic properties, have life times ranging from minutes to days, and their evolution is influenced by many atmospheric (meteorological) processes and varying environmental (aerosol) conditions, they are difficult to model and to be appropriately parameterized in atmospheric simulation models (Savre and Ekman, 2015; Solomon et al., 2018; Fridlind and Ackerman, 2018).

More life cycle studies are needed to accelerate progress in this important field of atmospheric research. The life cycle of a stratiform MPCs is controlled by two fundamental processes. The formation and maintenance of a droplet-dominated shallow cloud layer at the MPC top is of key importance. This steers all further processes that are required to explain the rather long MPCs lifetimes often observed in the Arctic. Emission of infrared radiation by the water droplets causes strong cooling at cloud top which leads to negative buoyancy at the rather stable conditions and subsequently to the evolution of a complex field of upward and downward motions below and within the liquid-dominated cloud layer (Shupe et al., 2008; Roesler et al., 2017). In areas with updrafts, existing droplets can grow and new droplets can form at water-supersaturation conditions. The steady supply of water droplets keeps the MPC top layer alive, frequently for hours, sometimes for several days (in the Arctic) as long as the humidity conditions are favorable (Morrison et al., 2012).

The second fundamental process is heterogeneous ice nucleation in the liquid-dominated cloud top layer, the subsequent growth of the ice particles, and the formation of extended ice virgae by falling ice crystals (Rauber and Tokay, 1991; Shupe et al., 2008; Ansmann et al., 2009; Morrison et al., 2012). The evolution of virga with growing and sublimating ice crystals in different parts of the fall strikes may further influence cloud dynamics and lifetime (Korolev and Field, 2008; Morrison et al., 2011; Eirund et al., 2019). Immersion freezing, i.e., ice nucleation on an ice-nucleating particle (INP) inside a supercooled water droplet, is the main ice nucleation mode (Ansmann et al., 2008, 2009), and preferably starts in the coldest region of the liquid cloud layer, i.e., at cloud top (Hobbs and Rangno, 1985), and preferably during updraft periods (Shupe et al., 2008; Ansmann et al., 2009). We would like to emphasize here that the first clear hint for the dominance of immersion freezing (compared to other ice nucleation modes) in stratiform MPCs was reported for subtropical and tropical MPCs (Ansmann et al., 2009), based on lidar observations during the SAMUM (Saharan Mineral Dust Experiment) campaigns (Ansmann et al., 2011). Motivated by the subtropical and tropical studies, this finding was confirmed for mid-latitudinal MPCs (Westbrook and Illingworth, 2011) and Arctic stratiform clouds (de Boer et al., 2011). Rauber and Tokay (1991) and (Shupe et al., 2008) already hypothesized that the liquid phase is obviously needed to trigger ice nucleation. Meanwhile, immersion freezing is well recognized as the mian ice nucleation mode in mixed-phase clouds (Boucher et al., 2013; Vali and Snider, 2015; Savre and Ekman, 2015; Fridlind and Ackerman, 2018; Solomon et al., 2018; Khain et al., 2022; Knopf et al., 2023). Further evidence for the predominance of the immersion freezing mode will be given in this article.

MPC life cycle monitoring is crucial to better understand the complex processes of MPC evolution and the impact of long-lasting MPC fields on other processes in the atmosphere and to improve the MPC parameterization in models. For a better monitoring of the liquid phase of stratiform clouds, we recently introduced the dual field-of-view (FOV) polarization lidar technique (Jimenez et al., 2020a, b). For the first time, important parameters of the liquid phase such as the effective radius

https://doi.org/10.5194/egusphere-2025-967
Preprint. Discussion started: 17 March 2025

$R_{\mathrm{e,liq}}$ and the cloud extinction coefficient α_{liq} can directly and accurately be determined from lidar observations. In addition, the liquid water content (LWC) can be computed by using the $R_{\mathrm{e,liq}}$ and α_{liq} information, and subsequently the cloud droplet number concentration (CDNC) can be well estimated (Jimenez et al., 2020a). Such a high quality characterization of the liquid phase is possible because of the sensitivity of such dual FOV observations to the droplet size, making the method more reliable than alternative single FOV approaches as the ones presented by Donovan et al. (2015) and Snider et al. (2017). These techniques depend on assumptions that permit only a rough estimation of the liquid-phase microphysical properties (Kalesse et al., 2016; Zhang et al., 2019). This fact was the motivation for the development of the new dual FOV lidar technique (Schmidt et al., 2013, 2014; Jimenez et al., 2020a, b). For the first time, we have a robust procedure to precisely monitor and characterize the liquid phase and the ice phase of MPCs simultaneously and thus to study the interplay between the two phases over long time periods in detail. The respective ice extinction coefficient α_{ice}, effective radius $r_{\mathrm{e,ice}}$, ice water content (IWC), and ice crystal number concentration (ICNC) are derived from combined lidar-radar observations (Bühl et al., 2019a; Ansmann et al., 2024a).

We present two Arctic case studies, one monitored during the central winter period (30-31 December 2019) and another case collected during the late summer season (21 September 2020) close to the North Pole in the framework of the MOSAiC (Multidisciplinary drifting Observatory for the Study of Arctic Climate) expedition, lasting from October 2019 to September 2020 (Engelmann et al., 2021; Shupe et al., 2022). We observed a strong disturbance of the MPC evolution on 21 September by three gravity waves and documented the surprisingly fast recovery of the liquid phase within a few hours after the perturbation. These two case studies demonstrate the unique capabilities offered by the MOSAiC ground-based active remote sensing supersite aboard the German ice breaker *Polarstern*, the main MOSAiC remote sensing platform. The coherent year-around MOSAiC observations allowed us to present a full year of statistics on geometrical, optical and microphysical properties of MPC systems in the central Arctic. The focus is on the liquid-phase properties. Silber and Shupe (2022) presented a MOSAiC summary regarding Arctic MPC occurrence, based on the year-around *Polarstern* radiosonde observations (with four sondes per day), and included an extended analysis of cloud-generating air mass properties based on backward trajectory computations.

The article is organized as follows: After an introduction in the MOSAiC *Polarstern* route, employed instruments, and applied data analysis methods in Sect. 2, a brief overview about the aerosol conditions in the free troposphere is given in Sect. 3, followed by two MPC life cycle case studies in Sect. 4. Further observations of MPCs in the free troposphere, conducted during the main summer months June and July 2020, are discussed in Sect. 4. The statistical results of Arctic MPC properties are presented in Sect. 5. Finally, in Sect. 6, we briefly provide some comments regarding the conceptual MPC life cycle model that covers all key processes and aspects of an MPC life cycle and was introduced by Shupe et al. (2008) and Morrison et al. (2012). We provide some new aspects gained from our MOSAiC observations. Concluding remarks are given in Sect. 7.

https://doi.org/10.5194/egusphere-2025-967
Preprint. Discussion started: 17 March 2025

2 MOSAiC instrumentation and observational products

2.1 Remote sensing aboard *Polarstern*

MOSAiC was the largest Arctic research initiative in history. The main measurement period lasted from the beginning of October 2019 until the end of September 2020. The goal of the MOSAiC expedition was to take the closest look ever at the Arctic as the epicenter of global warming and to gain fundamental insights that are key to better understand global climate change. A rather detailed monitoring of the atmosphere, cryosphere and biosphere in the Central Arctic was realized. Most of the MOSAiC observations were conducted at latitudes >85°N (from the beginning of October 2019 to the beginning of April 2020, and from mid-August to the end of September 2020). Observations during the summer season (mid-May to mid-August) were performed at latitudes from 79-82°N, north and northwest of Svalbard, Norway.

Our role in the MOSAiC consortium was to provide a seasonally and height-resolved characterization of aerosols and clouds in the North Pole region from the surface up to 30 km height (Engelmann et al., 2021; Ohneiser et al., 2021, 2023; Ansmann et al., 2023, 2024a, b; Griesche et al., 2024b). We even illuminated a potential role of stratospheric wildfire smoke on polar ozone depletion (Ohneiser et al., 2021; Ansmann et al., 2022) and the relationship between vertically integrated tropospheric water vapor and the downward, broadband thermal-infrared irradiance at the ground during the MOSAiC winter half year (Seidel et al., 2024).

The German icebreaker *Polarstern* (Knust, 2017) served as the main MOSAiC platform for advanced remote sensing studies of the atmosphere (Shupe et al., 2022). *Polarstern* was trapped in the ice and drifted with the pack ice through the Arctic Ocean from 4 October 2019 to 16 May 2020. The entire cruise of the *Polarstern* is shown in Shupe et al. (2022). Our state-of-the-art combined aerosol-cloud Raman and dual FOV polarization lidar (Engelmann et al., 2016; Jimenez et al., 2020b) aboard *Polarstern* was operated side by side with the ARM (Atmospheric Radiation Measurement) mobile facility 1 (AMF-1), which conducted cloud radar observations. The containerized multiwavelength lidar is routinely operated aboard the *Polarstern* since more than 15 years (Kanitz et al., 2011; Bohlmann et al., 2018; Yin et al., 2019; Griesche et al., 2020).

Ground-based active remote sensing with advanced lidars and cloud radars permits the study life cycles of stratiform MPC systems coherently over hours to days (Shupe, 2007; Shupe et al., 2008; Illingworth et al., 2007; de Boer et al., 2011; Bühl et al., 2016; Kalesse et al., 2016; Achtert et al., 2020; Griesche et al., 2020; Radenz et al., 2021b; Engelmann et al., 2021). Sophisticated retrieval methods (e.g., Delanoë and Hogan, 2008; Schmidt et al., 2013; Sourdeval et al., 2018; Bühl et al., 2019a; Jimenez et al., 2020a; Mason et al., 2023) allow for a detailed derivation of cloud micropyhsical properties. Meanwhile, also lidar-based aerosol retrieval methods are introduced to cover the aerosol part in cloud process studies (Mamouri and Ansmann, 2016; Marinou et al., 2019; Ansmann et al., 2019a, 2021; Choudhury and Tesche, 2022; Choudhury et al., 2022; He et al., 2023). The dual FOV Raman lidar technique (Schmidt et al., 2013) and the recently introduced dual FOV polarization lidar technique (Jimenez et al., 2020a) were developed to better study the life cycles of stratiform clouds with focus on the liquid phase and the impact of aerosols on the microphysical properties of stratiform, droplet-dominated cloud layers (Schmidt et al., 2014, 2015; Jimenez et al., 2020b). The new dual FOV polarization lidar technique was integrated into the MOSAiC Raman lidar (Engelmann et al., 2021), right before the start of the MOSAiC (Multidisciplinary drifting Observatory for the

https://doi.org/10.5194/egusphere-2025-967
Preprint. Discussion started: 17 March 2025

Study of Arctic Climate) expedition (Shupe et al., 2022) to significantly improve the remote sensing capabilities for Arctic MPC studies. The remote sensing station aboard *Polarstern* performed continuous measurements during the entire one-year MOSAiC expedition without any break.

Besides the lidar observations we made use of the ARM cloud radar measurements to derive profiles of ice crystal properties of the MPC systems by combining lidar and radar data. The 35 GHz Doppler cloud radar (Ka-band ARM Zenith Radar, KAZR) of the ARM mobile facility AMF-1 of the US Department of Energy (http://www.arm.gov, last access: 22 November 2024) measures radar reflectivity, mean Doppler velocity, and Doppler spectrum width (ARM, 2024).

We also used the observations of the liquid water path (LWP) with the radiometer HATPRO (Humidity and Temperature Profiler) microwave radiometer (Rose et al., 2005; Griesche et al., 2024b). Finally, we used the dense set of radiosonde temperature and relative humidity profiles (Maturilli et al., 2021) in our cloud studies. Vaisala radiosondes (type RS41) were launched regularly every 6 hours aboard *Polarstern* throughout the entire MOSAiC year.

2.2 Lidar products

An overview of all measured and retrieved lidar products, used in this study, together with typical uncertainties are listed in Table 1. The uncertainties given in the table result from error propagation studies, but especially from numerous validation efforts as discussed in several of our MOSAiC papers before (see, e.g., Ansmann2023). The basic lidar data analysis applied to obtain the geometrical and optical properties (backscatter, extinction, linear depolarization ratio) is outlined in Baars et al. and Hofer et al. (2017). The main features of the MOSAiC-related aerosol data analysis (including signal correction, Rayleigh backscattering and extinction correction, temporal averaging and vertical smoothing of signal profiles) are described in Ohneiser et al. (2020, 2021, 2022). Relative humidity fields, as shown in Engelmann et al. (2021), Seidel et al. (2024), and in Sect. 4 are obtained from Raman lidar observations of the water-vapor-to-dry-air mixing-ratio profiles (Dai et al., 2018) and temperature profiles measured with the *Polarstern* radiosondes. In this computation, the temperature profiles are required with a resolution of 30 s and obtained by linear interpolation between the radiosonde data for each height bin, given for fixed times (6, 12, 18, and 24 UTC). Quality checks were based on comparisons with the MOSAiC radiosonde humidity profiles (Seidel et al., 2024).

The retrieval of aerosol microphysical properties such as the aerosol particle number concentrations and surface area concentration, listed in Table 1, as well as of estimates of cloud-relevant properties such as the cloud condensation nucleus (CCN) and ice-nucleating particle (INP) number concentrations is performed by means of the POLIPHON (Polarization Lidar Photometer Networking) approach (Mamouri and Ansmann, 2016, 2017). Lidar input data sets are the height profiles of the 532 nm backscatter coefficient and the particle depolarization ratio. We determined conversion factors (for the conversion of measured optical properties into microphysical properties) even for Arctic aerosol conditions during the summer half year (Ansmann et al., 2023). The particle number concentration n_{50}, considering all particles with radius >50 nm, is used as proxy for the CCN concentrations, and n_{250}, considering the large particle fraction (particles with radius >250 nm), is used to indicate the reservoir of INPs. More details to the lidar retrievals are given in Ansmann et al. (2023). We assume that mineral dust is the most favorable INP type in the free troposphere in the Arctic and contributes with 1% to the large particle fraction so that the

https://doi.org/10.5194/egusphere-2025-967
Preprint. Discussion started: 17 March 2025

Table 1. Overview of the MOSAiC lidar-derived and lidar-radar retrieved aerosol and cloud products and typical relative uncertainties in the determined and retrieved properties. r denotes aerosol particle radius. Optical properties (extinction coefficient, depolarization ratio) are given for 532 nm.

Aerosol and cloud properties	Uncertainty
Aerosol 532 nm extinction coefficient [Mm^{-1}]	20-25%
Aerosol 532 nm depolarization ratio	5-10%
Aerosol particle surface-area conc. [μm^2 cm^{-3}]	$\leq$25%
Aerosol particle number conc. ($r >$50 nm) [cm^{-3}]	factor of 2
Aerosol particle number conc. ($r >$250 nm) [cm^{-3}]	$\leq$25%
Ice-nucleating particle number concentration [L^{-1}]	factor of 3
Cloud droplet extinction coefficient [Mm^{-1}]	15-20%
Cloud droplet depolarization ratio	$<$5%
Cloud droplet number concentration [cm^{-3}]	25-75%
Cloud droplet effective radius [μm]	15%
Liquid water concentration [μg m^{-3}]	25%
Ice crystal extinction coefficient [Mm^{-1}]	25%
Ice crystal depolarization ratio	$<$5%
Ice crystal number concentration [L^{-1}]	factor of 2-3
Ice crystal effective radius [μm]	35%
Ice water concentration [μg m^{-3}]	60%
Water vapor mixing-ratio [g kg^{-1}]	5-10%
Relative Humidity	10%

INP reservoir is $0.01 \times n_{250}$. This assumption is supported by global airborne aerosol observations presented by Froyd et al. (2022).

In this article, the focus is on our one-year MOSAiC observations of stratiform clouds, occurring in the lower and middle free in the height range from 500 m to 7 km. The recently introduced dual FOV polarization lidar method (Jimenez et al., 2020a, b) is based on the measurement of the volume linear depolarization ratio at two different FOVs. The depolarization ratio is defined as the ratio of the cross-polarized to the co-polarized backscatter coefficient. "cross" and "co" indicate the plane of polarization orthogonal and parallel to the plane of linear polarization of the transmitted laser pulses. The volume depolarization ratio monotonically increases from zero at cloud base to values > 0.2 within the cloud layer due to multiple scattering of laser light by the cloud droplets. The multiple scattering effect is a strong function of the number concentration of cloud droplets, their size, as well as of the receiver FOV of the lidar. By measuring the multiple scattering effect (via light depolarization) with two FOVs we are able to unambiguously derive the single-scattering cloud extinction coefficient α_{liq} and the effective radius $R_{\mathrm{e,liq}}$, i.e., the geometrical-cross-section-weighted mean radius of the droplets from the dual FOV lidar observations. The derived extinction coefficients can be cross-checked by single-scattering droplet backscatter coefficients

https://doi.org/10.5194/egusphere-2025-967
Preprint. Discussion started: 17 March 2025

(multiplied by the water cloud lidar ratio of 18 sr) obtained from elastic backscatter signals. In the next step, we calculate the liquid water content, LWC, as a function of the cloud extinction coefficient and effective radius and, finally, the cloud droplet number concentration, CDNC, from LWC by assuming a gamma size distribution. The most accurate set of solutions is obtained at heights of 50-100 m above the base of the liquid-dominated cloud layer of the MPC (Jimenez et al., 2020b; Engelmann et al., 2021). In situ observations (Mioche et al., 2017) indicate that such observations in the lower part of the liquid-dominated cloud layer represent well the liquid phase properties of shallow MPCs. The uncertainty analysis shows that the lidar approach, originally developed for pure water clouds, can be applied even to MPCs as long as the contribution of backscattering by ice crystals to the total backscatter coefficient is clearly below 5% in the cloud top layer (Engelmann et al., 2021). During MOSAiC, the ice backscatter fraction was always of the order of 1-2% or less.

2.3 Lidar-radar products

Information about ice crystal properties such as the ice crystal number concentration (ICNC) and ice water content (IWC) can be obtained from the combination of Ka-band ARM Zenith Radar (35 GHz cloud Doppler radar) and 532 nm backscatter lidar observations (Bühl et al., 2019a; Ansmann et al., 2024a). Table 1 includes the MPC ice-phase properties. Since lidar observation of pure ice crystal backscattering is only available for the virga zones, the retrieval is restricted to the height range below the liquid-dominated MPC top layer. For a close comparison with the liquid phase properties (obtained for 75 m above cloud base) we used the ice phase properties obtained from the lidar-radar retrievals at 250 m below the cloud base of the MPC top layer. According to the airborne in situ MPC observations of Mioche et al. (2017), these virga observations are well representative for the entire MPC height range, including the liquid-dominated cloud top layer.

The applied LIRAS-ice (LIdar RAdar Synergy - retrieval of ice microphysical properties) analysis scheme (Bühl et al., 2019a; Ansmann et al., 2024a) was originally developed and applied to investigate the impact of Saharan dust on mixed-phase and ice clouds over the Eastern Mediterranean (Ansmann et al., 2019b) and also used in Arctic cirrus formation studies (Ansmann et al., 2024a). LIRAS-ice makes use of the measured profiles of the radar reflectivity factor Z (8.5 mm wavelength) and of the ice crystal extinction coefficient α_{ice} at 532 nm wavelength. Accurate 532 nm ice single-scattering extinction coefficients are of fundamental importance to retrieve high quality, trustworthy products. Very accurate α_{ice} profiles are obtained by means of the Raman lidar method. In the first step, the height profile of the single-scattering ice crystal backscatter coefficient is determined by using a modified version (Baars et al., 2017; Jimenez, 2021) of the Raman lidar method (Ansmann et al., 1992). In the second step, the backscatter profile is multiplied with the well known single scattering 532 nm ice crystal lidar ratio (extinction-to-backscatter ratio) of around 32 sr to get the required profile of the single-scattering ice crystal extinction coefficient α_{ice}. For more details (including references for cirrus lidar ratio observations and retrievals) we refer to Ansmann et al. (2024a) and to the articles of Bühl et al. (2019a) and Ansmann et al. (2019b).

Complementary to the dual FOV lidar products for the liquid phase the LIRAS products are the ice extinction coefficient α_{ice}, the effective radius $R_{\mathrm{e,ice}}$, IWC, and ICNC. The ice water path (IWP, vertically integrated IWC) is calculated from the IWC values in the ice virga plus the IWC values in the liquid-dominated cloud top layer. Here, we use the virga IWC value at the top of the virga zone to be representative for the entire liquid-dominated cloud top layer as well and thus assume a height

https://doi.org/10.5194/egusphere-2025-967
Preprint. Discussion started: 17 March 2025

constant IWC profile from cloud base to the top of the cloud layer (obtained from the radar reflectivity observations). The liquid water path LWP is finally computed from the observations with the HATPRO (Humidity and Temperature Profiler) microwave radiometer (Rose et al., 2005).

2.4 MPC statistics: data analysis procedure

In Sect. 5, we show statistical results of liquid-phase properties of Arctic liquid-bearing cloud layer in the free troposphere. The analysis is solely based on the dual FOV polarization lidar observations in the free troposphere (at heights above 500 m) from October 2019 to September 2020. In the first step, we removed all lidar observations that showed fog and low cloud conditions. These data cannot be analyzed properly because the laser light is quickly attenuated and the rather strong backscatter signals partly overload the detectors. About 3760 hours (44%) of the MOSAiC measurement time period showed low clouds and fog. After applying several quality assurance procedures to the lidar observations, we selected around 360 hours of observations of well-defined stratiform cloud events, obtained during fog and low-cloud-free conditions, for our studies. In the next step, we calculated 7 minute mean signal profiles. Based on 3070 individual cloud profiles (7 minute averages) we computed the droplet-related optical and microphysical properties of the stratiform cloud layers. The data analysis covered the height range from 500 m to 7 km height.

We distinguish pure liquid-water clouds (PL clouds) and MPCs in Sect. 5. All clouds showing virga structures below the cloud top layer were defined as MPCs. Those clouds, which produced no detectable virgae, were classified as pure liquid-water clouds. Cloud base and top heights were obtained from the lidar backscatter and depolarization observation (base heights) and from the radar reflectivity measurements (top heights). The MOSAiC radiosonde temperature data were finally used to assign cloud top temperatures, i.e., the temperatures at which heterogeneous ice nucleation usually starts.

We show statistics regarding the temporal length of the measured cloud fields. The temporal length is given by the time an individual cloud layer needs to cross the lidar site. We defined cloud layers as single, individual layers, when they were detected at different heights. In the case of a broken cloud fields (many cloud segments at the same height level), we counted a cloud field as one single cloud system if the detected cloud-free periods lasted for less than an hour. If a cloud-free period exceeded 60 minutes, the next cloud field, crossing *Polarstern* at that height level, was counted as a new cloud. The results presented in Sect. 5 only consider clouds with temporal length $>$15 minutes.

3 MOSAiC free tropospheric aerosol conditions

We briefly illuminate the CCN and INP reservoirs in the lower free troposphere over the Arctic during the MOSAiC year. Fig. 1 shows the aerosol particle number concentrations n_{50} (a proxy for the CCN concentration) and of n_{250} (large particle fraction which contains the INP reservoir). The retrieval of these particle number concentrations are explained in detail in Ansmann et al. (2023). During the MOSAiC year, values for n_{50} and n_{250} mostly ranged from 20-200 cm^{-3} and 100–1000 L^{-1} at heights around 2 km, respectively. According to the INP discussion in Ansmann et al. (2023) and the global dust observations by Froyd

https://doi.org/10.5194/egusphere-2025-967
Preprint. Discussion started: 17 March 2025

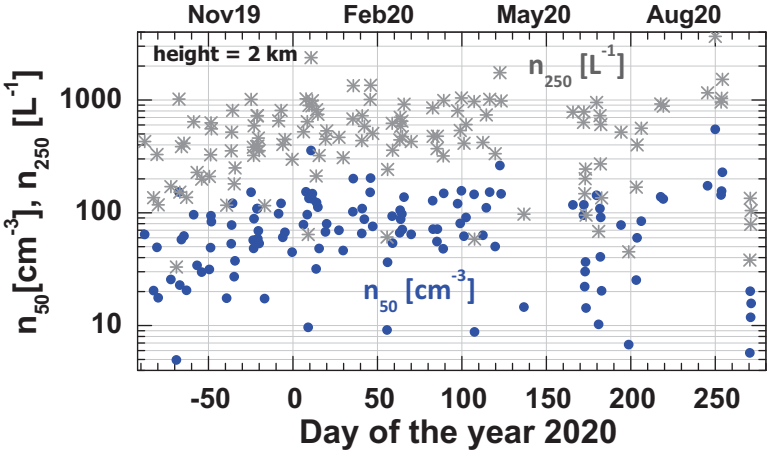

Figure 1. Lidar-derived particle concentration n_{50} (in blue, particle with radius >50 nm, proxy for CCN concentration) and n_{250} (gray stars, particles with radius >250 nm) for the height level of 2000 m. The full MOSAiC year from October 2019 to September 2020 is covered by lidar observations. A fraction of 1% of n_{250} may be dust particles, which form the INP reservoir. Dust particles are assumed to be the only ice-active particles in winter and also widely control heterogeneous ice nucleation in the free troposphere in summer. The uncertainty in the lidar estimates is 25% in the case of n_{250} and a factor of 2 in the case of n_{50}.

et al. (2022) it is reasonable to assume that traces of dust, of the order of 1%, contribute to n_{250} in the free troposphere. These dust particles form the INP reservoir as defined by Knopf et al. (2023).

The estimated INP concentration values in the lower free troposphere (at 2 km height), presented in Ansmann et al. (2023), were mostly in the range from 0.005-0.02 L^{-1} during the winter period (November 2019 to April 2020) for the temperature of -25°C, a 1% dust fraction, and a time interval of ice nucleation of 60 s. For a cloud top temperature of -30°C (as discussed in the next section) and a typical updraft duration (ice nucleation period) of the order of 3-5 minutes, INP concentrations increase to 0.1-1 L^{-1}. An estimation of the free tropospheric INP concentration at summer conditions is difficult because of the unknown impact of non-dust INPs that may nucleate ice crystals already at frequently occurring cloud top temperatures of -5 to -15°C. At these high temperatures, mineral dust particles are ice-inactive. All in all, Fig. 1 provides the impression that the CCN and INP reservoirs in the lower free troposphere were almost always well filled.

4 MOSAiC MPC case studies

We begin with two long-lasting MPC events. During the polar winter half year we frequently observed MPC events that lasted for many hours, and in several cases even longer than a day. The longest period of 5.5 days with quasi continuous MPC evolution was observed in November 2019. The two long-lasting MPC cases will be discussed in Sect. 4.1-4.2. We selected a cold, mid-winter case (29-31 December 2019) with a text-book-like MPC evolution (in Arctic haze) over more than 27 hours and a late summer case (21 September 2020) which developed in a wildfire smoke- and anthropogenic haze-polluted

https://doi.org/10.5194/egusphere-2025-967
Preprint. Discussion started: 17 March 2025

environment. The summer observation contains an unexpected feature, namely the strong perturbation of the MPC evolution by three lofting events with amplitudes of 100-300 m. Gravity waves may have caused the perturbations. This specific event allowed us to study the interaction between the liquid and the ice phase in unique detail and how stable, equilibrium-like cloud conditions were reached again after several hours. Besides the discussion of the two long-lasting winter and summer MPC events, we provide insight into the Arctic MPC characteristics during the main summer months of June and July 2020 in Sect. 4.3. As an outlook, in Sect. 5, we finally summarize our MPC observations and present statistical results for the MOSAiC year with focus on the liquid phase.

4.1 29-31 December 2019 MPC life cycle

4.1.1 Macrophysical properties and meteorological conditions

A very stable MPC deck was observed over *Polarstern* on 30-31 December 2019. The results are presented in Figs. 2 to 4. The *Polarstern* was at 86.6°N and 116°-118°E and drifted with the pack ice. No local orographic effect perturbed the MPC evolution. The cloud system crossed the *Polarstern* with a mainly westerly wind component. The radiosonde observations indicated wind velocities of 4-6 m s^{-1} from the surface up to 4 km height. Satellite imaginary (Worldview-earthdata-nasa-2024) showed a more than 500 km times 200 km large MPC field in the North Pole region on 30 December 2019. By applying the aerosol source identification scheme of Radenz et al. (2021a), the air mass at 1-3 km height was advected from latitudes $>$60°N, and a few percent from 30-60°N, most likely from the North American continent and crossed partly snow-free regions and thus contained some soil material. Arctic haze pollution, however, dominated the aerosol conditions in the lower free troposphere in the central Arctic during the MOSAiC winter months (Engelmann et al., 2021; Ansmann et al., 2023).

An overview of the macrophysical cloud properties and meteorological conditions are given in Fig. 2. The droplet-dominated cloud top layer developed in a moist air mass between 2 and 3 km height. The vertical extent of the cloud top layer (in red in Fig. 2b) was 300-400 m according to the 5 and 17 UTC radiosonde humidity profiles in Fig. 2c. The relative humidity over water RH_w reached 100% in the droplet containing top layer. The yellow stream-like structures in Fig. 2b are produced by virgae of falling ice crystals. Almost no windshear and low windspeeds allowed an undisturbed evolution of the ice virgae. The virgae got thinner with time and the vertical extent decreased when the air mass became drier below 2 km height after 12 UTC on 30 December 2020 (see Fig. 2d). We assume that each virga is related to an individual updraft event during which CCN activation as well as ice nucleation preferably takes place (Shupe et al., 2008; Khain et al., 2022).

After the formation and establishment of an opaque liquid top layer, a strong drop in the temperature of the MPC top layer occurred, as the comparison of 23 UTC with the 5 and 17 UTC radiosonde temperature profiles in Fig. 2a indicate. The strongest temperatures decrease was found at cloud top. The temperature decreased from around -27°C (radiosonde launch at 23 UTC) to -32°C (radiosonde launched at 5 UTC) at 2.8-2.9 km height as a result of the strong emission of long-wave radiation by the cloud top layer. The strong radiative cooling leads to decreased static stability in the cloud top layer and buoyant production of turbulence within and below the cloud top layer (Roesler et al., 2017) and to the evolution of regular pattern of updraft and downdraft periods (Shupe et al., 2008). In the continuously occurring updrafts, CCN activation and condensational growth of

https://doi.org/10.5194/egusphere-2025-967
Preprint. Discussion started: 17 March 2025

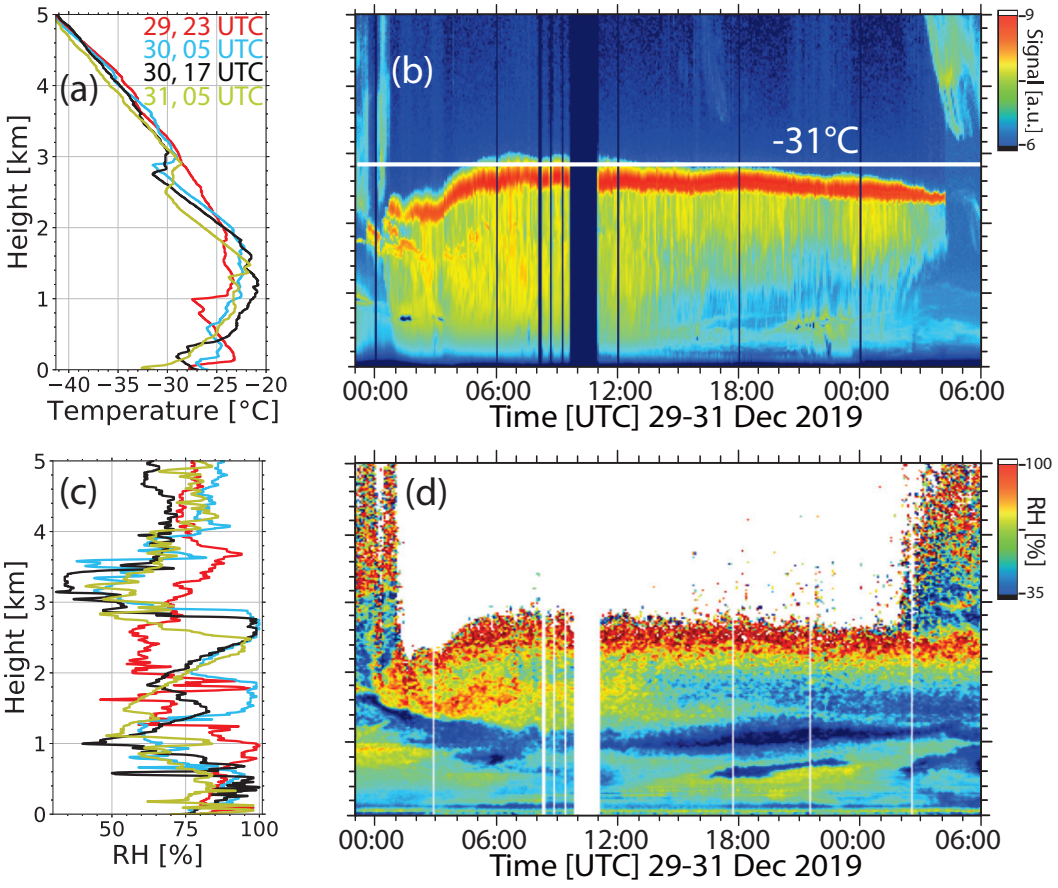

Figure 2. Life cycle of a MPC observed with Raman lidar aboard *Polarstern* at 86.6°N, 116-118°E, on 30-31 December 2019 (panel b). The height-time display of the 1064 nm range-corrected signal in panel b shows the droplet-dominated cloud top layer (in red) between 2 and 3 km height. Virgae (in yellow) of falling ice crystals develop and partly reach the ground. Profiles of temperature (panel a) and relative humidity (over water, panel c) were measured with four MOSAiC radiosondes launched at 23 UTC (29 December), 5 and 17 UTC (30 December) and 5 UTC (31 December 2019). Thin black vertical lines in panel b indicate times of radiosonde profiles. Cloud top temperature was between −30 and −32°C. In panel d, the relative-humidity field computed from water-vapor mixing-ratio profiles measured with lidar and temperature profiles measured with radiosonde are shown. Several dark bars in panel b and white bars in panel d indicate times with now useful lidar observations (partly caused by automated calibration and adjustment events). In panel d, the large white area above the MPCs indicates missing lidar data. In panels b and d, the lidar observations are biased in the near range (<250 m).

existing droplets takes place. The longevity of the MPC deck is, to our opinion, the result of the continuous production of liquid water, especially of the formation of new droplets.

https://doi.org/10.5194/egusphere-2025-967
Preprint. Discussion started: 17 March 2025

The humidity conditions on 30-31 December 2019 over the *Polarstern* are shown in Fig. 2d. Blue and red colors indicate low relative humidity of $<40\%$ and values of 100%, respectively. The lidar measures the water-vapor mixing ratio with a vertical resolution of 7.5 m and a temporal resolution of 30 s. By using the MOSAiC radiosonde temperature profiles (available with a resolution of 6 hours), the mixing ratio profiles were converted into relative humidity profiles (see Sect. 2.2 for more details).

Pronounced lofting of the air mass (until about 7:00 UTC on 30 December) caused water supersaturation and the formation of the cloud top layer (in red in Fig. 2b). Strong ice nucleation and crystal growth started immediately in the droplet environment at favorable immersion freezing temperatures below -30°C (and corresponding ice saturation ratio $S_{\mathrm{i}} > 1.34$) at cloud top. Intense and extended virgae of falling ice crystals developed and reached low heights. Sublimating ice crystals kept the relative humidity high between the cloud top layer and 1 km height until 14:00 UTC. Cooling of the air during the sublimation processes may contribute to a strong downward motion of ice-containing air layers. With time the advected air mass became significantly drier. However, sublimation of crystals were able to keep the relative humidity high in a 300-400 m thick layer below the droplet-dominated top layer. The released water vapor, CCNs, and INPs may have partly been transported back into the cloud top layer during updraft periods. Further CCNs and INPs may have entered the cloud from above, from below via blowing snow effects (Gong et al., 2023), or were advected within the moist air mass with the prevailing westerly windflow. Increasing cooling of the MPC top layer also leads to an increase of available INPs.

The cloud top layer became thinner (optically and geometrically) so that water vapor observations were possible again (as in the beginning) up to 4-5 km height. The updraft-downdraft circulation system weakened and finally collapsed so that the MPC dissolved at 4:00 UTC. The 6 UTC radiosonde (launched at 5 UTC) indicated water subsaturation at all heights and maximum values around 90% at 2.5 km height.

4.1.2 Microphyscial properties: ice phase vs liquid phase

The retrieval products for the liquid and the ice phase are presented in Fig. 3. The three height-time displays in Fig. 3a, 3b, and 3c show the basic lidar and radar observations. The cloud radar provides an overview of the MPC life cycle in terms of the radar reflectivity Z (caused by ice crystals at 8 mm wavelength in Fig. 3a). The radar detects all ice crystals in the vertical tropospheric column. Even the ice virgae originating from upper tropospheric cirrus clouds above the MPC are detected. These crystals may have influence the MPC evolution via the feeder-seeder effect (Rauber and Tokay, 1991; Ansmann et al., 2008, 2009; Ramelli et al., 2021) before 7 UTC on 30 December 2019. According to the radar observations, the top height of the MPC was at about 3 km height. The nucleated ice crystals grow and fall out of the MPC liquid-dominated cloud top layer and form large virgae. Riming processes (Waitz et al., 2022) may have contributed to strong ice production in the liquid-dominated cloud top layer. Since the radar is more sensitive to large hydrometeors such as ice crystals, which are usually quite homogeneously distributed over the entire MPC height range (down to the virga base height), the base of the liquid-dominated cloud top layer remains undetected in the radar reflectivity height-time display in Fig. 3a. The black dots, shown in Fig. 3a are indicating the cloud base. This information is taken from the lidar observations.

The lidar precisely detects the base of the liquid-dominated clout top layer, given as white circles in Fig. 3b. However, the lidar is usually unable to detect the top of this cloud layer because of strong attenuation of laser light by droplet scattering

https://doi.org/10.5194/egusphere-2025-967
Preprint. Discussion started: 17 March 2025

processes. Cloud top heights can be detected as long as the cloud optical depth COD $\leq$ 2.5. However, in most cases COD is $>$ 5. The ice extinction coefficient in the ice virgae (at 532 nm wavelength, below the white dots in Fig. 3b) is obtained by multiplying by the highly resolved backscatter coefficients with a typical ice crystal lidar ratio of 32 sr (see discussion in Ansmann et al. (2024a, b)).

Figure 3c shows the observations of the depolarization ratio. The depolarization ratio permits a clear separation of the droplet-dominated cloud top layer and the ice crystal virga zone. High values (yellow to red) of the depolarization ratio indicate ice crystal backscattering, and low values (dark blue to green) droplet backscattering. In the cloud top layer, the depolarization ratio monotonically increases from almost zero (at the base of the liquid-dominated cloud top layer) to values close to 0.2 by the increasing contribution of multiple scattering by cloud droplets to the backscattering intensity.

When zooming into the virga zone in Fig. 3a to 3c, singular, individual virgae with pronounced backscattering and depolarization features can easily be identified. The regularly occurring virga structures are the result of enhanced ice production during the updraft periods (Shupe et al., 2008). During upwind phases, the conditions for both CCN activation and droplet growth as well as ice nucleation and crystal growth are most favorable, while during downdraft periods, only ice crystal growth (Wegener-Bergeron-Findeisen (WBF) mechanism) (Korolev, 2007) and sedimentation continues to occur (Khain et al., 2022). We counted 30-35 individual virga structures within 6 hour intervals (12-18 UTC, 18-24 UTC on 30 December 2019), i.e, updrafts occurred every 10-12 minutes. Taking the radiosonde observations of the horizontal wind speed of about 5 m s^{-1} up to 4 km height into considerations, the updraft phases were horizontally separated by about 3 to 3.5 km from each other. Similar horizontal scales of the updraft-downdraft periods were observed by Shupe et al. (2008). Note that during the late summer MPC event, observed on 21 September and discussed in Sect. 4.2, 40-60 virgae occurred within six hours and point to horizontal separations of updraft zones by only 1.8-2.2 km. Horizontal wind velocities were again around 5 m s^{-1}.

In Fig. 3d to 3g, the retrieval products for both, the liquid and the ice phase are given as time series. The liquid phase values are obtained by means of the new dual FOV lidar method for the height of 75 m above cloud base. One of the two measured depolarization ratios is shown in Fig. 3c. The ice extinction coefficient and the microphysical properties for the ice phase are given for the height of 250 m below the base of the droplet-dominated cloud layer and derived from combined lidar-radar observations shown in Fig. 3a and 3b. According to the observations of Mioche et al. (2017), these values at about 75 m above cloud base (liquid phase) and 250 m below cloud base (ice phase) can well be used to describe the overall characteristics of shallow Arctic MPCs.

The results in Fig. 3 clearly show that we resolved well all main phases of the entire life cycle of the MPC system. However, we are aware of the fact that caution has to be exercised in studies of cloud life cycles (Lagrangian perspective) by analyzing Eulerian measurements (measurements at a fixed location) (Fridlind and Ackerman, 2018; Grabowski, 2020; Khain et al., 2022)). We can identify and distinguish three phases of the MPC evolution. During the initial phase with large-scale lofting until 8:00 UTC on 30 December 2019, the optical and microphysical properties (except the effective radius) of both phases are quite variable. This variability is probably partly related to the potential impact of seeder-feeder effects. In seeder-feeder processes, the ice crystal seeds enter a liquid cloud from above and grow fast on the expense of liquid water droplets which evaporate during the ice growth process. The radar observations in Fig. 3a show a strong virga field above the MPC until 6 UTC

https://doi.org/10.5194/egusphere-2025-967
Preprint. Discussion started: 17 March 2025

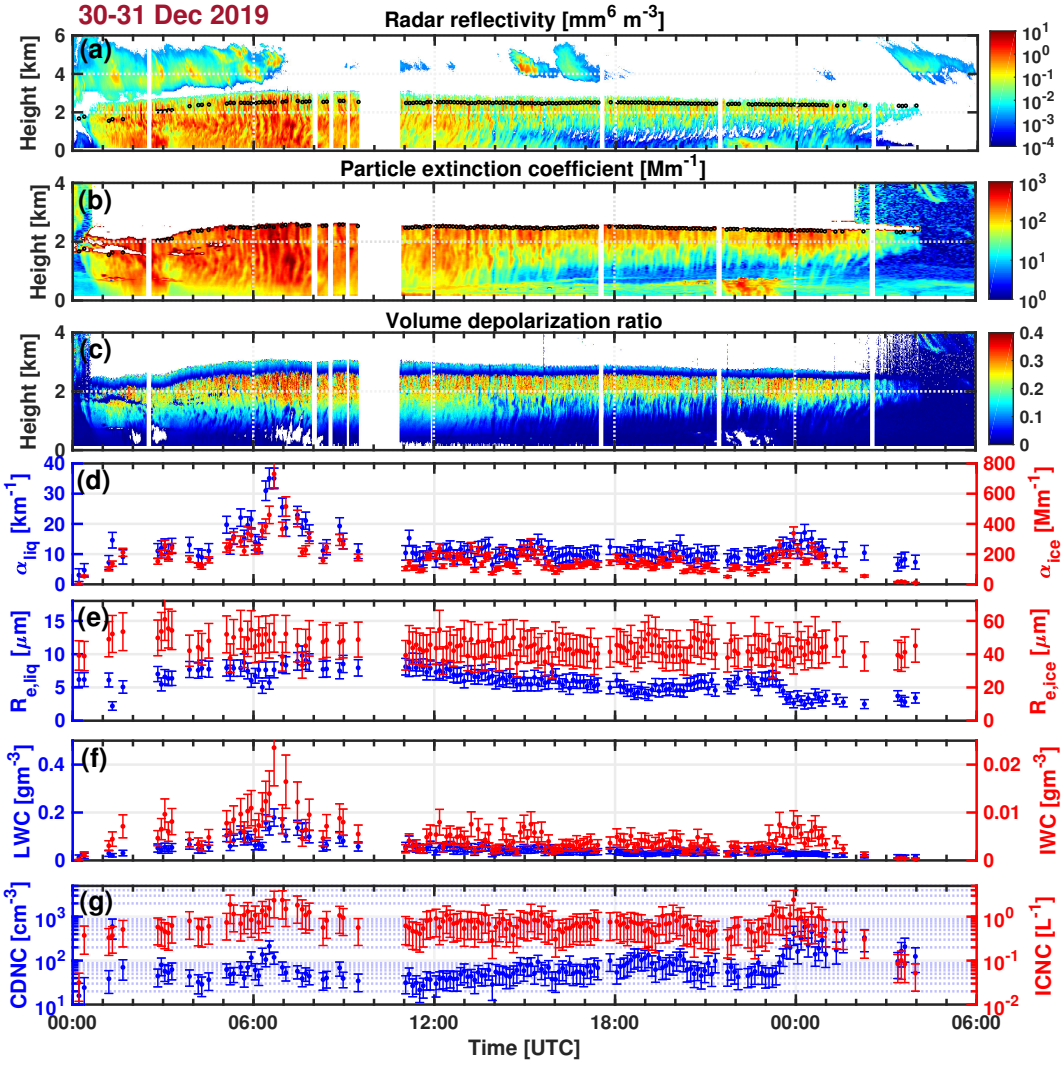

Figure 3. Life cycle of a MPC as observed (a) with cloud radar (radar reflectivity Z) and (b, c) with lidar (panel b: particle extinction coefficient α_{ice}, panel c: volume depolarization ratio) aboard *Polarstern* at 86.6°N on 30-31 December 2019. Black dots in (a) and white dots in (b) show the base of the liquid-dominated cloud top layer as detected with lidar. Time series of (d) the droplet extinction coefficient (in blue) and the ice crystal extinction coefficient (in red), (e) the effective radii of droplets (blue) and ice crystals (red), (f) LWC (blue) and and IWC (red), and (g) CDNC (blue) and ICNC (red) are retrieved by using the basic observations in panels (a), (b), and (c). The droplet properties (in blue) are computed for the height of 75 m above the base of the liquid-dominated cloud top layer. The ice properties (in red) are determined in the virga zone at 250 m below the base of the liquid-dominated cloud top layer. SD bars indicate the uncertainty in the retrieval products. Gaps in the time series, associated with white vertical columns in (a) to (c) indicate missing data.

so that ice crystals could in principle enter the MPC from above (as ice seeds). The additional ice production may have caused the intensification of ice virga backscattering during the initial phase of the MPC lifetime.

https://doi.org/10.5194/egusphere-2025-967
Preprint. Discussion started: 17 March 2025

The main and second phase of the life cycle (from about 8:00 UTC to 23:00 UTC), is characterized by a stable liquid-dominated cloud deck which controls the further evolution of the MPC system. The third and final phase of the MPC life cycle, observed after 23:00 UTC on 30-31 December 2019 was caused by the decreasing water vapor content and decreasing turbulent motion in the advected air mass, as already mentioned above and shown in Fig. 2. All processes such as cloud top cooling and the evolution of pronounced updrafts and downdrafts, required to allow for strong CCN activation and droplet growth, weakened, and finally the chain of processes collapsed, and the cloud deck dissolved.

During the stable phase, the liquid-phase and ice-phase extinction coefficients show values around 10 km^{-1} and 0.1-0.2 km^{-1}, respectively. The effective droplet radius slowly decreased from 8 μm to 5 μm, and the ice crystal effective radius was around 40 μm. LWC and IWC values were on average 0.05 g m^{-3} and 0.003 g m^{-3}, respectively. For the number concentrations, CDNC and ICNC, we obtained values from 30-150 cm^{-3} and between 0.5 and 1 L^{-1}, respectively. In terms of LWC and IWC, the ice-phase fraction (Korolev et al., 2017) was thus about 0.06. In terms of the optical properties α_{liq} and α_{liq}, the ice-phase fraction was 0.01-0.02. When using the number concentrations, CDNC and ICNC, we end up with an ice phase fraction of the order of 10^{-5} to 10^{-6}. That means only a rather small fraction of the droplets was involved in immersion freezing processes.

The almost time-constant properties from 11:00-23:00 UTC on 30 December indicate rather stable conditions of ice nucleation and growth. INPs may have been entrained continuously from above and from below or advected with the main air flow. A depletion of the INP reservoir is not visible. The most surprising observation is the steady increase of the CDNC from values around 30 cm^{-3} at 11:00-11:30 UTC to values above 100 cm^{-3} at 19:00 UTC, and, at the same time, the decrease of the effective droplet radius from 8 to 5 μm. This is surprising because the continuously occurring processes of ice growth by water vapor deposition, associated with shrinking and evaporation of droplets, should lead to a reduction of the droplet number concentration and, in addition, to a decrease of the effective droplet radius. Droplet-droplet collision and coalescence processes may cause a less strong reduction of the effective radius but contributes together with riming processes to a reduction of CDNC. It cannot be excluded that the observed changes in the CDNC and $R_{\mathrm{e,liq}}$ numbers may be simply related to changing aerosol conditions by advection or entrainment processes, however, to our opinion, the observation of an increasing CDNC and, simultaneously, decreasing effective droplet radius $R_{\mathrm{e,liq}}$ with time is a clear sign that CCN activation occurred and permanently refilled the small droplet fraction and stabilized in this way the broad droplet size distribution. Our hypothesis of a strong role of droplet nucleation in the lifetime of MPCs is in line with model results of Khain et al. (2022). Based on simulations with their 2D Lagrangian-Eulerian mixed-phase cloud model, Khain et al. (2022) also found that ice particles at concentrations < 1 L^{-1} do not affect the LWC in the liquid-dominated cloud top layer significantly. Cloud-top glaciation (via the WBF mechanism) is possible when ICNC exceeds 10 L^{-1}, i.e., only when ICNC >10 L^{-1}, the WBF process has a strong impact on the conversion of cloud liquid water to ice water. As can be seen in Fig. 3g, ICNC was mostly in the range of 0.3-1 L^{-1}. A comparably weak WBF process contributes to favorable conditions for strong CCN activation.

It is worthwhile to mention that long-lasting MPC events as observed on 30-31 December 2019 are favorable cases to demonstrate (by using a large-eddy-simulation-informed MPC aerosol-cloud model) that a time-dependent ice nucleation mechanism paired with a large INP reservoir can sustain continuous ice crystal production for several hours (Knopf et al., 2023). The

https://doi.org/10.5194/egusphere-2025-967
Preprint. Discussion started: 17 March 2025

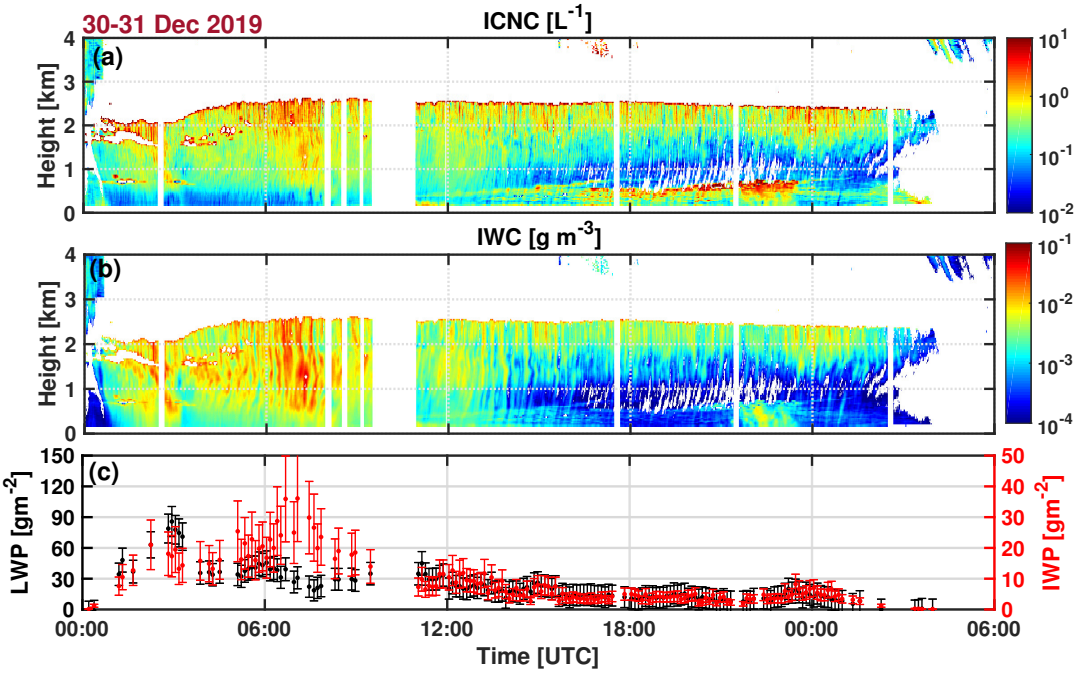

Figure 4. Evolution of the MPC observed on 30-31 December 2019 in terms of (a) the ice crystal number concentration (ICNC), (b) ice water content (IWC), and (c) liquid water path (LWP, in blue) and ice water path (IWP, in red). Error bars show the uncertainty in the retrieved LWP and IWP values. White vertical columns indicate periods without lidar data. The uppermost red rim of the data field in panel a is a bias and occurs at the base (sharp edge) of the liquid-dominated cloud layer, The lidar extinction values start to be influenced by strong water droplet backscattering here.

longevity of such clouds, sustaining both liquid and ice crystal formation over a long time period, is poorly represented across global climate models when using a time-independent approach to characterize INP activation. The underlying freezing parameterization defines the number of ice-nucleating particles (INPs) available for ice formation, termed INP reservoir. A time-dependent freezing description yields a substantially greater INP reservoir than time-independent approaches, and therefore greater ice formation over long time periods.

Figure 4 finally presents height-time displays of ICNC (panel a) and IWC (panel b) and shows time series of the liquid water path LWP and the ice water path IWP in Fig. 4c. The retrieval of LWP and IWP was described in the last paragraph of Sect. 2.3. ICNC and IWC decreased with decreasing height in the virga zone during the stable phase of the life cycle after 12:00 UTC. This height dependence is the result of sublimation of crystals. As long as the virgae do not reach the ground the released water vapor and particles are available to be transported back into the cloud-top layer and to act again as CCNs and INPs. The IWP ranges from 10-35 g m^{-2} during the initial phase of the MPC life cycle (before 11 UTC) and was very constant for the rest of the MPC lifetime with values around 5 g m^{-2}. The LWP was most of the time <35 g m^{-2}, and around 15 g m^{-2} during the

https://doi.org/10.5194/egusphere-2025-967
Preprint. Discussion started: 17 March 2025

second and third phase of the MPC lifetime. In terms of LWP and IWC, the ice-phase fraction (IWP/(IWP+LWP)) was thus of the order of 0.25.

The observed properties for this mid-winter MPC event agree well with respective findings obtained from airborne in situ measurements conducted in the framework of several Arctic aircraft campaigns (in the spring seasons of 2004, 2007, 2008 and 2010) north and around Svalbard (78°N, 15°E), Longyearbyen, Norway and Kiruna (68°N, 20°E), Sweden (Mioche et al., 2017). The MOSAiC December MPC showed slightly lower values compared to airborne in situ spring observations. In numbers, the spring time Arctic MPCs showed in situ measured droplet extinction coefficients of 20±10 km^{-1}, a droplet effective radius around 7.5 μm, and LWC and CDNC values of 0.2±0.1 g m^{-3} and 120±60 cm^{-3}, respectively. For the ice phase, Mioche et al. (2017) found extinction coefficients of about 0.4±0.3 km^{-1}, effective ice crystal radius of 50±25 μm, IWC of 0.03±0.03 g m^{-3} and ICNC of 3±2 L^{-1}.

The observations on 30-31 December 2019 agree also well with long-term lidar-radar observations over Leipzig from 2011 to 2015. Bühl et al. (2016) shows LWP, IWC, and and ice phase ratio (IWC/LWC) as a function of the MPC top temperature. At -30°C, IWC ranged from 10^{-6} to 5×10^{-6} kg m^{-3}, LWP were of the order of 0.01 kg m^{-2} for MPCs with cloud top temperatures of -30°C, and the respective ice phase ratio IWC/LWC showed values around 0.03-0.05. During the stable phase of the MPC life cycle we observed LWP of 0.015 kg m^{-2} on 30 December 2019, IWC of 3×10^{-6} kg m^{-3}, and for the IWC/LWC ratio we obtained 0.003 to 0.06.

4.2 21 September 2020 MPC life cycle

In this section, we discuss the life cycle of a long-lasting late-summer MPC event that was observed over the North Pole on 21 September 2020. *Polarstern* was drifting within an ice field at 88.5°N. The results for this case are given in Figs. 5-7. As on 30-31 December 2019, the air mass came from Iceland, Greenland, northern Canada, and even from Alaska. In contrast to the December 2019 case study, the cloud top temperatures were around $-22.5°$ to -23.5°C (at 3.3-3.4 km height) according to the radiosondes launched at 11 and 17 UTC on 21 September 2020. The cloud layer was thus warmer by 8-10 K than the one in December 2019. A drop by 2 K at 3.3 km height from 5 UTC (cloudless conditions) to 11 UTC was observed due to radiative cooling of the liquid-dominated cloud top region. Anthropogenic pollution and wildfire smoke from Siberia and North America were advected into the central Arctic since mid-July 2020 (Boyer et al., 2023; Heutte et al., 2024; Ansmann et al., 2023). In addition, soil dust and mineral dust, probably predominantly from nordic sources (e.g., from Iceland) as well as biological aerosol particles (locally produced or advected from the Arctic surrounding continents) contributed to the Arctic aerosol mixture in the free troposphere during the MOSAiC summer half year. The larger amount of condensate (in the warmer cloud) and the higher CCN concentration caused much larger liquid-phase-related cloud extinction coefficients and higher CDNC values in the cloud top layer than in December 2019 as will be discussed below.

A strong perturbation of the cloud evolution occurred at 12:00 UTC, and was probably the result of a gravity wave crossing *Polarstern*. This noon event is highlighted in Fig. 5. The sudden ascent of the MPC top layer significantly disturbed the development of the liquid and the ice phase of the MPC deck and the interaction between both phase for hours. Besides the

https://doi.org/10.5194/egusphere-2025-967
Preprint. Discussion started: 17 March 2025

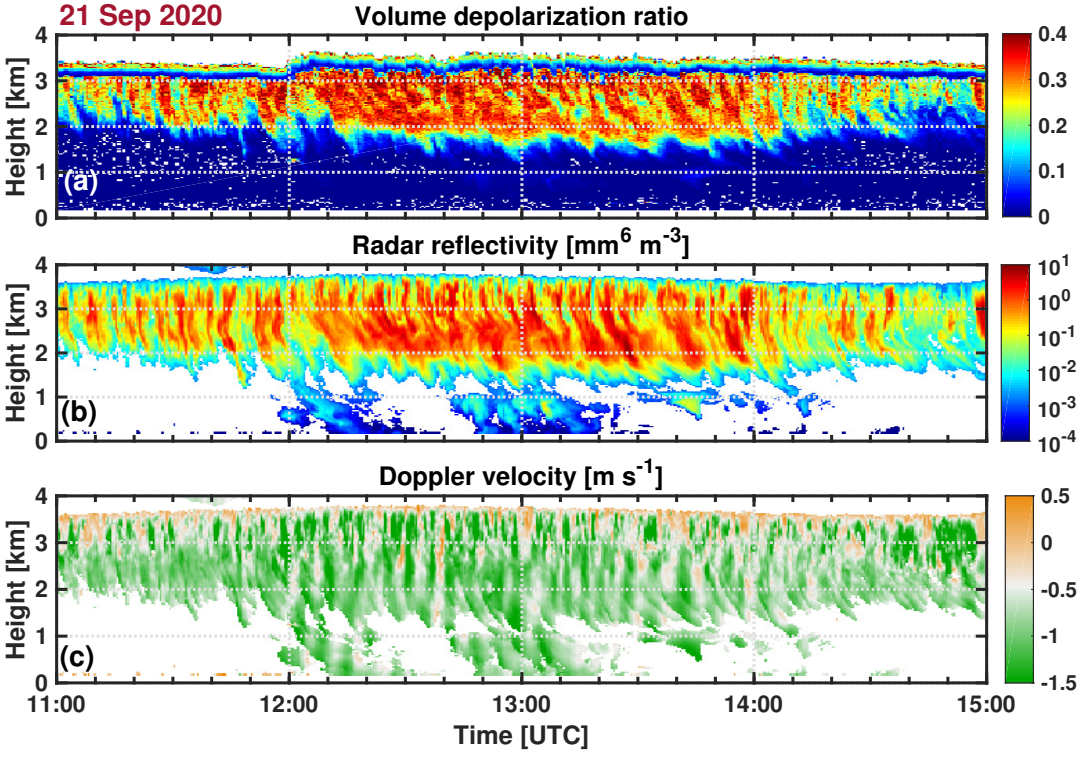

Figure 5. Perturbations of the MPC development on 21 September 2020 at 12:00 UTC, visible in the lidar observations of the volume depolarization ratio in (a). In (b), the cloud radar reflectivity Z and, in (c), the vertical velocity derived from the cloud Doppler radar observations are shown. The sudden height change of the dark blue band above 3 km height in (a), i.e. of the liquid-dominated cloud layer, by 250-300 m was probably initiated by a gravity wave. In (c), vertical velocities > -0.5 m s^{-1} are highlighted in grey to orange colors. The orange regions may indicate upwind areas when taking permanent ice crystal sedimentation into account.

perturbation at 12:00 UTC, two weaker events took place at 12:40 UTC and around 13:40 UTC as a careful and detailed inspection of all our observational data and retrieval products indicated.

A clear impact of the 12:00 UTC lofting event on the cloud structures is visible in Fig. 5a. The base height of the liquid-dominated cloud top layer (see the blue band indicating a depolarization ratio of zero caused by strong droplet backscattering) was initially lofted by 150-200 m and further ascended by another 100 m probably as a result of condensation of water vapor on existing droplets and ice crystal nucleation and growth and related heat release. The lofting process was completed in less than 10 minutes. The 12:00 UTC perturbation triggered an intensification of ice production and broadened the virga structures. A significantly stronger backscattering by ice crystals in the virga zone was detected after 12:10 UTC. The virga activity became weaker again after 14 UTC, after the impact of the second and third perturbations on the MPC evolution, occurring around 12:40 and 13:40 UTC.

https://doi.org/10.5194/egusphere-2025-967
Preprint. Discussion started: 17 March 2025

The respective cloud radar observation of this 12:00 UTC event is shown in Fig. 5b. Note again, that the cloud radar reflectivity mostly contains information about ice crystals. As in the case of the lidar backscatter, the radar reflectivity Z increased in the virga zone after 12:10 UTC (until 14:00 UTC). In addition, three precipitation fields appeared in the height-time display of the radar reflectivity below the main virga zone, in phase with the perturbation at 12:00, 12:40, and around 13:40 UTC. The ice crystal concentration must have been rather low in these precipitation fields because the lidar did not detect these features in the depolarization measurements in Fig. 5a. An expected pronounced lofting of the air mass at 12:00 UTC is not visible in the radar data. The only weak hint on the 12:00 UTC perturbation is the increase of the virga top height (red color, close to the top of the liquid-dominated cloud layer) from about 3.4 km before 12:00 UTC to 3.6 km at times later than 12:10 UTC.

In Fig. 5c, we show the vertical-velocity component derived from the Doppler radar observations. We were expecting that the Doppler velocity would show the lofting event most clearly. However, this is not the case as can be seen. Besides the continuously visible crystal sedimentation impact (negative velocities, green colors), the regular structures of upward and downward motions (permanently initiated by radiative cooling of the cloud top region) dominated the measured Doppler shifts and derived wind information. For a better identification of potential lofting areas, we shifted the color scale by 0.5 m s^{-1} so that the neutral grey color shows weak negative velocities around -0.5 m s^{-1} and orange colors velocities > -0.25 m s^{-1}. However, the only vertical columns (5 minute periods), almost without any green color and therefore suggesting a lofting event, occurred at 12:00 and 12:40 UTC.

The full life cycle of the MPC system observed on 21 September 2020 is shown in Fig. 6. To remind, the liquid phase properties were obtained by applying the recently introduced dual FOV lidar technique (by using the observations in panel c) whereas the ice phase properties were retrieved by the synergistic lidar-radar data analysis (by using the observations shown in panels b and c).

During the first perturbation (lofting) phase around 12:00 UTC, strong growth of the existing droplets and probably also strong droplet collision and coalescence as well as riming processes occurred caused by enhanced turbulent motion (Bühl et al., 2019b). As a consequence of droplet growth and coalescence events the effective droplet radius increased from 5 μm to 7.5 μm, with some values $>$10 μm, LWC increased from 0.08 to 0.2 g m^{-3}, and the CDNC decreased from about 200 cm^{-3} to 70-80 cm^{-3} and continued to decrease, probably as a result of strong ice production. Cooling by 2-3 K caused a strong enhancement of ice nucleation (roughly by a factor of 5), growth of new and of the already existing ice crystals, and intensification of the ice virga structures. The ice extinction coefficient (in the virga zone, 250 m below the liquid-dominated cloud layer) increased from 0.1-0.2 to 0.6 km^{-1}, the ice water content IWC from around 0.005 to 0.016 g m^{-3}, and the ICNC from around 0.5 to 2-3 L^{-1}. The stable phase in the MPC evolution could not establish before 15:00 UTC. After 15:00 UTC and the fall out of the large amount of ice crystals, ice production was significantly reduced for the rest of the MPC lifetime.

The most impressive result is the recovery of the liquid phase during the afternoon hours. The CDNC dropped from 200-300 cm^{-3} at 10:00-12:00 UTC by an order of magnitude and showed values around 30 cm^{-3} at 13:30 UTC, and then recovered to 200-300 cm^{-3} at 15:00-16:00 UTC. For the effective droplet radius, we found values of 5 μm at 11:00 UTC, maximum values close to 15 μm at about 13:00 UTC, and then later on values again around or just below 5 μm at 16:00 UTC. These strong and coherent changes in the CDNC and $R_{\mathrm{e,liq}}$ time series during the phase with strong perturbations can only consistently

https://doi.org/10.5194/egusphere-2025-967
Preprint. Discussion started: 17 March 2025

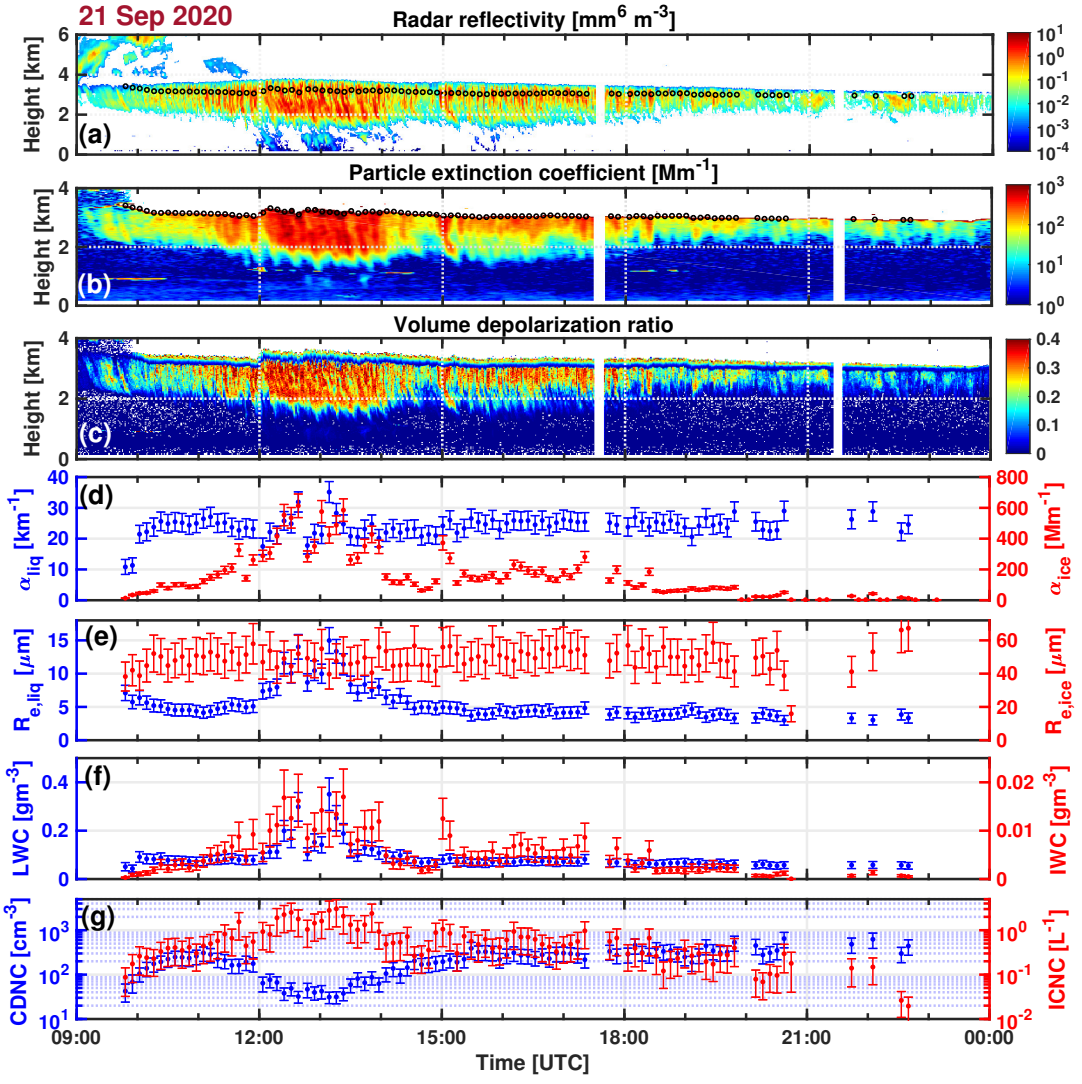

Figure 6. Same as Fig. 3, except for 21 September 2020. *Polarstern* was at 88.5°N. Black dots in (a) and (b) show the base of the liquid-dominated cloud top layer. The three perturbations at 12:00, 12:40, and 13:40 UTC disturbed the evolution of the liquid phase (blue, d-g) and the ice phase (red, d-g) properties significantly.

be explained when taking strong CCN activation into considerations. The alternative hypothesis that changes in the cloud properties are simply the result of changing aerosol conditions is not convincing.

During the main and stable phase of the MPC lifetime, the ice extinction coefficients showed values around 0.1-0.15 km^{-1} and the ice crystal effective radius was around 50 μm. LWC and IWC values were about 0.08-0.1 g m^{-3} and 0.003-0.005 g m^{-3}, respectively. For the number concentrations, CDNC and ICNC, the values ranged mostly from 200-300 cm^{-3} and between 0.1 and 1 L^{-1}, respectively. In terms of LWC and IWC, the ice-phase fraction was thus about 0.04-0.05. By using the optical

https://doi.org/10.5194/egusphere-2025-967
Preprint. Discussion started: 17 March 2025

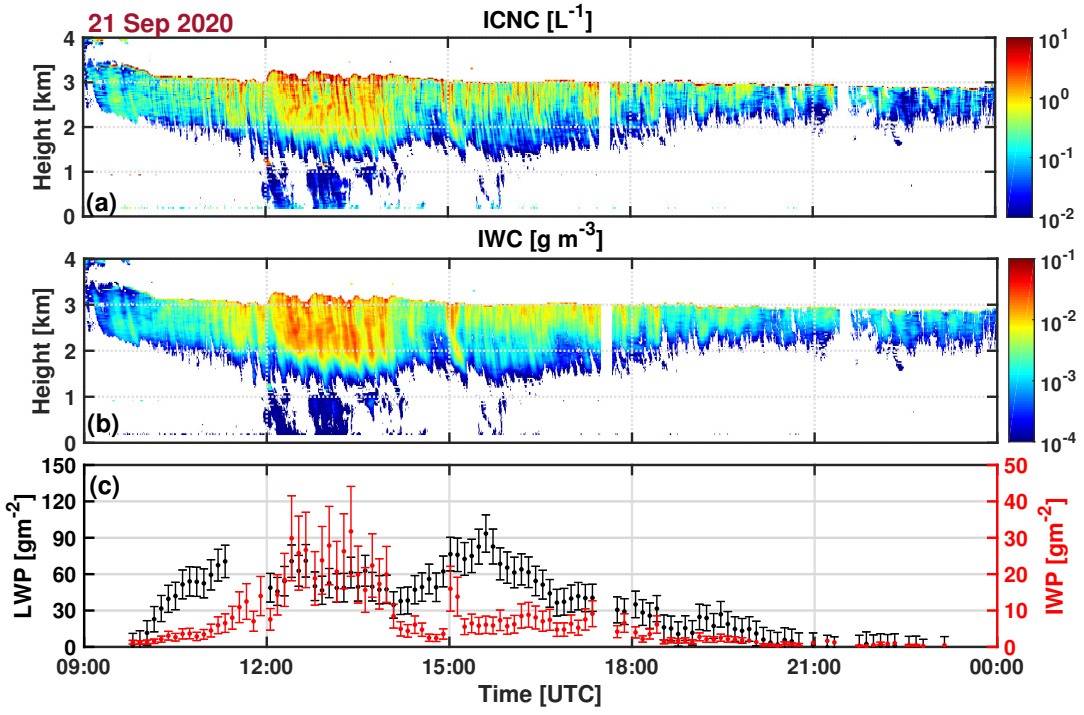

Figure 7. Same as Fig 4, except for 21 September 2020. Gravity waves crossed *Polarstern* between 12:00 and 14:00 UTC and prodcued strong ice virgae and triggered strong ice production.

properties α_{liq} and α_{liq}, the ice-phase fraction was 0.006. With the number concentrations, CDNC and ICNC, we end up with an ice phase fraction of the order of 2×10^{-6}.

Figure 7 shows time series of LWP and IWP (in panel c), together with height-time displays of ICNC (panel a) and IWC (panel b). LWP decreased only slowly with time, from values as high as 90 g m^{-2} at 16:00 UTC to values around 30 g m^{-2} at 18:00 UTC. IWC, on the other hand, was already mostly $<$ 10 g m^{-2} after the perturbation period ending at 14:00 UTC and remained low for the rest of the MPC lifetime. Accordingly, the ice-phase fraction was about 0.05 (at 16:00 UTC) and 0.15 (at 18:00 UTC) in terms of LWP and IWP. The precipitation signatures at heights below 1 km show rather low ICNC values close to 0.01 L^{-1} and LWCs close to 0.0001 g m^{-3}. This is the reason why these features remained undetected in Fig. 5a.

4.3 June-July 2020 MPC observations

During the MOSAiC summer months of June and July, low level clouds and fog below 300-500 m height covered the sky above *Polarstern* in 50-55% of the time. In winter, the respective percentage was 35%. At such conditions, useful lidar observations can not be performed. However, even during summer there were many measurement periods and opportunities to study MPCs in the free troposphere at heights >500 m and to characterize the MPCs in terms of optical and microphysical properties. In the following, we present the results for two episodes measured in June and in July 2020. The *Polarstern* cruised between 78° and

https://doi.org/10.5194/egusphere-2025-967
Preprint. Discussion started: 17 March 2025

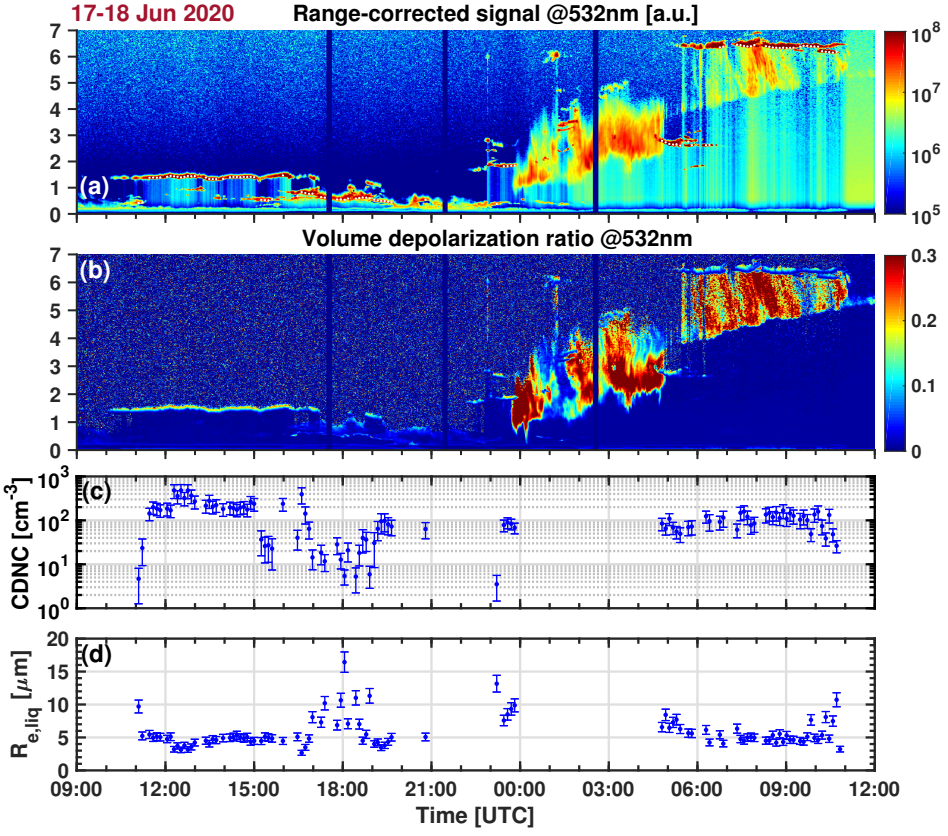

Figure 8. Lidar observations of liquid water clouds (before 00:00 UTC of 18 June 2020) and MPCs with strong virga evolution (after 00:00 UTC) in terms of (a) range-corrected 532 nm backscatter signal and (b) volume depolarization ratio. White dots in panel a indicate the cloud base height of cloud segments for which the cloud droplet number concentration (CDNC, panel c) and the effective droplet radius $R_{\mathrm{e,liq}}$ (panel d) is derived from the dual-FOV polarization lidar observations. Error bars indicate the uncertainty in the products. All cloud layers show a blue color at cloud base (not always visible) in panel b, in an unambiguous sign for liquid-dominated cloud layers so that ice is produced by immersion freezing. The strong increase of the depolarization ratio with height (from blue to light greem yellow or even red) is caused by multiple light scattering by the water droplets. The large red areas in panel b indicate ice virgae.

82°N north and northwest of Svalbard, Norway, from mid-May to mid-August 2020. Daytime conditions were given around the clock. Figs. 8 and 9 show the two summertime MPC periods with cloud layers at many different height levels from the surface to 6.5 km. We use the opportunity here again to highlight the potential of the new dual FOV polarization lidar technique which was used for the first time during the MOSAiC expedition to continuously monitor pure liquid-cloud as well as MPC properties.

Most of the free-tropospheric clouds were short-lived with lifetimes from 20 minutes to less than 3 hours. Two longer lasting cloud events were measured for about 5-6 hours on 17-18 June (Fig. 8) and several events (broken cloud fields) were monitored over 5-15 hours on 25-28 July2020 (Fig. 9). Droplet number concentrations in the stratiform clouds ranged from values around

https://doi.org/10.5194/egusphere-2025-967
Preprint. Discussion started: 17 March 2025

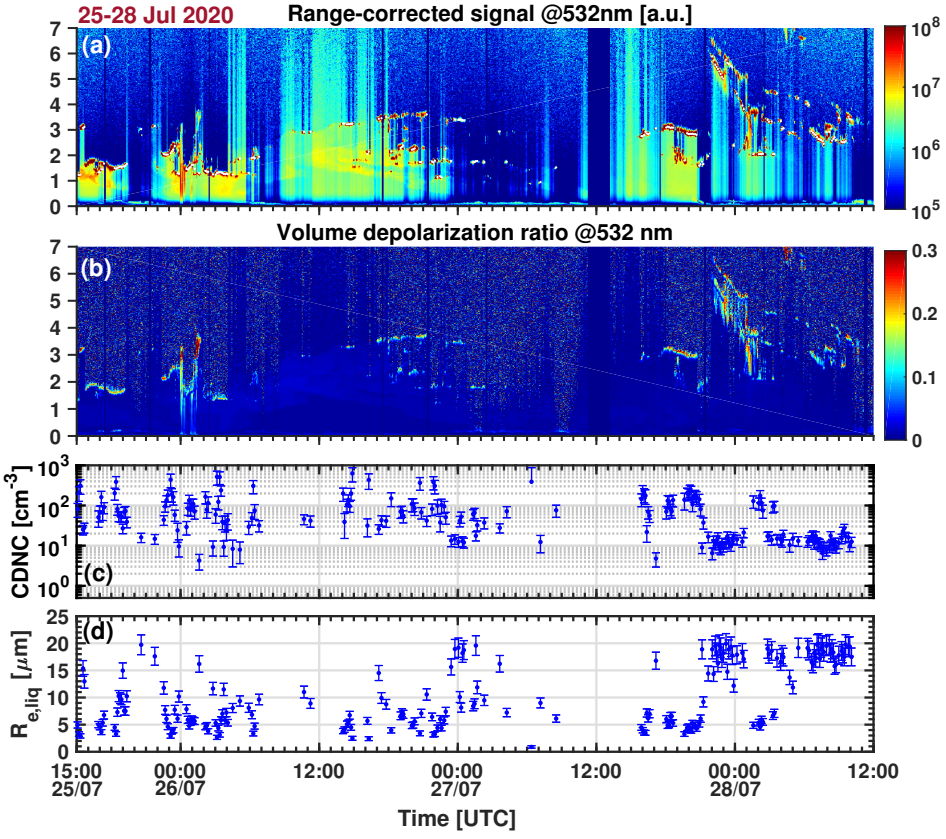

Figure 9. Same as Fig. 8, except for the time period from 25-28 July 2020. Many short-lived stratiform cloud layers are detected (see white dots indicating cloud base height). Only a few of these clouds produced ice.

10 cm^{-3} in clean air to values of several 100 cm^{-3} in clouds developing in polluted air (typically prevailing in the free troposphere). The CDNC values directly reflect the aerosol pollution conditions with respectively high CCN concentrations of several 100s per cm^3. Biomass burning smoke from wildfires in Siberia, Canada and Alaska as well as anthropogenic pollution contributed to the aerosol burden in June and especially in late July 2020 (Boyer et al., 2023; Heutte et al., 2024). The effective droplet radius was mostly around 5 μm, but also showed values of 15-20 μm in Fig. 8 and 9 (in panels c and d). It should be mentioned here that the dual FOV lidar technique was optimized for cloud scenarios with effective radii up to 16 μm so that the uncertainties in the effective radius values $>$ 16 μm are larger than indicated by the errors bars in Fig. 8 and 9.

All detected MPC layers showed rather low depolarization values at the base of the cloud top layer (unfortunately not well visible in Fig. 8 and 9). These low depolarization ratios are an unambiguous sign for a liquid-dominated cloud layer (and backscattering by spherical particles) and that immersion freezing is the only active ice nucleation mode (Ansmann et al., 2009; Westbrook and Illingworth, 2011; de Boer et al., 2011). A strong ice formation period on 18 June 2020, from about midnight to 12 UTC. A warm and moist air mass reached *Polarstern* in the late evening of 17 June 2020. Intense ice nucleation started

https://doi.org/10.5194/egusphere-2025-967
Preprint. Discussion started: 17 March 2025

around 23:30 UTC. It remains unclear at what height ice nucleation was initiated, at 4 km (at −13°C), 5 km at (at −20°C), or at 6 km (at temperatures close to −30°C). The 24 UTC radiosonde measured relative humidity (over water) reaching 100% only at 5.8-6 km height at temperatures of −29° to −30°C. It seems to be most likely that the lower clouds were seeded from above and the intense virgae developed by the rapidly growing ice seeds in the lower MPC layers.

The 6 UTC radiosonde (18 June) then showed a layer with 100% relative humidity between 2.65 and 2.75 km height at −8°C. The lidar observations did not indicate ice nucleation in this cloud layer. The CDNC values ranged from 30-100 cm^{-3} and the effective droplet radius from 5 to 7.5 μm at that time. Another cloud layer with 100% humidity was found at 6.4-6.5 km with temperatures of −31.6° to −32.2°C in the 6 UTC radiosonde data. Strong ice nucleation and ice virga formation was detected with lidar. The virga crystals sublimated when reaching a drier air mass at heights below 4-5 km height so that seeding of lower clouds was not possible after 5 UTC on 18 June 2020. Mineral dust particles were probably responsible for strong ice nucleation in the air mass above 6 km height.

The second period with pure liquid clouds and MPCs, discussed here, lasted from 25 to 28 July 2020. Two short ice nucleation events were observed in this week (see Fig. 9), one after midnight on 26 July, 00:00-01:00 UTC, and one around midnight of 27-28 July (22:00-02:00 UTC). The 23 UTC radiosonde (25 July) indicated a moist layer from about 4-4.3 km height with temperatures from −4.6° to −6.8°C. There was no further moist layer higher up, indicating cloud formation. No cirrus developed on this day, the atmosphere was very dry above 6.5 km height (with relative humidity <10%) so that seeder-feeder events could not develop. This very short ice nucleation event was no longer visible in the next humidity profile of the radiosonde launched at 5 UTC. In this specific case again non-dust INPs may have triggered ice nucleation at quite high ice nucleation temperatures. In the case of the ice nucleation event from 22:00 UTC on 27 July to 02:00 UTC on 28 July 2020, the 24 UTC radiosonde detected a moist layer from 5.8-6.4 km height at temperatures from −19.5°C to −24°C. Ice virgae (and associated seeder-feeder effects) were observed with lidar down to 2 km height. Mineral dust is the most favorable INP type at these low temperatures.

5 MOSAiC MPC liquid-phase statistics

Silber and Shupe (2022) analyzed 1362 RH profiles measured with MOSAiC radiosondes between 4 October 2019 and 19 September 2020. The sondes were launched from *Polarstern* with a resolution of six hours. The authors found that 997 RH profiles (73%) contained signatures of liquid-bearing cloud layers and in 50% of these profiles (37% out of all radiosonde profiles) multi-layer cloud structures were found, i.e., liquid-bearing cloud layers from the surface up to the middle free troposphere.

Our continuous lidar observations aboard *Polarstern* provided complementary information. In about 2630 h (31%) out of the 8450 MOSAiC measurement hours (from 4 October 2019 to 21 September 2020), near-surface low-level clouds and fog were observed during 710 h (17% of the time) of the winter half year (before 1 April 2020) and 1920 h (46% of the time) of the summer half year. Free tropospheric lidar measurements are not possible at these conditions. Such a high low-cloud and fog occurrence frequency (at heights <500 m) is typical for the Arctic in summer (Achtert et al., 2020; Griesche et al.,

https://doi.org/10.5194/egusphere-2025-967
Preprint. Discussion started: 17 March 2025

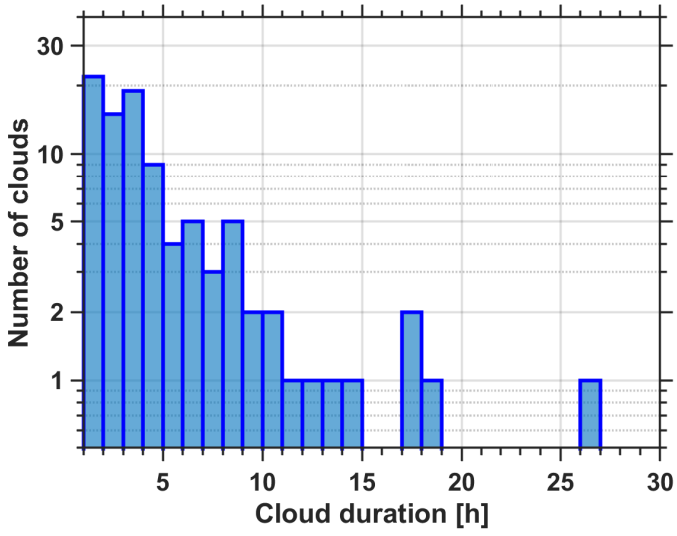

Figure 10. Frequency distribution of individual, coherently observed cloud layers as a function of the time period, needed by the cloud field to cross the *Polarstern*. We analyzed 94 individual cloud fields, measured within 360 h during the MOSAiC year from October 2019 to September 2020.

2024a). According to Achtert et al. (2020), the cloud occurrence frequency drops from values close to 50% to 20-25% for free tropospheric liquid-bearing clouds (at heights >500 m in the Arctic). We may thus conclude for the MOSAiC time period that during the 5800 MOSAiC hours of low-cloud and fog-free conditions in about 1300-1400 h free tropospheric clouds occurred.

We selected a subset of 360 h (out of these 1300-1400 h) and analyzed 94 individual cloud layers by means of the dual FOV lidar method. About 190 h out of the 360 h of cloud observations were conducted during the pack ice drift from October 2019 to mid-May 2020 (pure liquid clouds, PL: 70 h, MPCs: 120 h) and 170 h of cloud observations were performed from mid-May to September 2020 (main summer season, PL clouds: 131 h, MPCs: 39 h). A careful data quality check with special focus on properly aligned dual FOV receiver characteristics was applied to all of the selected cloud events.

Figure 10 provides an overview of the temporal lengths of these 94 cloud events, i.e., of the time periods the individual clouds fields needed to cross *Polarstern*. Cloud layers with a temporal length of less than 20 minutes are not considered in Fig. 10. In about 60% out of the 94 cloud events, we observed clouds layers (from the beginning to the end of the *Polarstern* crossing time) with temporal lengths of < 3 h. In about 10% out of all analyzed cases (including the cloud events on 30-31 December 2019 and 21 September 2020), the observations lasted for more than 10 h. Shupe et al. (2006) analyzed a one-year cloud data set of 284 identified Arctic liquid-bearing clouds measured between October 1997 and September 1998. They found typical occurrence (measurement) lengths of 2-12 h, with median and mean values of 6 h and 12 h, respectively. 30% out the analyzed almost 300 cloud cases showed temporal lengths of < 3 h.

In Fig. 11a, b,d, and e, the dual FOV lidar products are shown. The 3070 analyzed cloud profiles (based on 7 minute signal averages) served as the basis for the statistical analysis. The liquid-phase-related optical and microphysical cloud properties,

https://doi.org/10.5194/egusphere-2025-967
Preprint. Discussion started: 17 March 2025

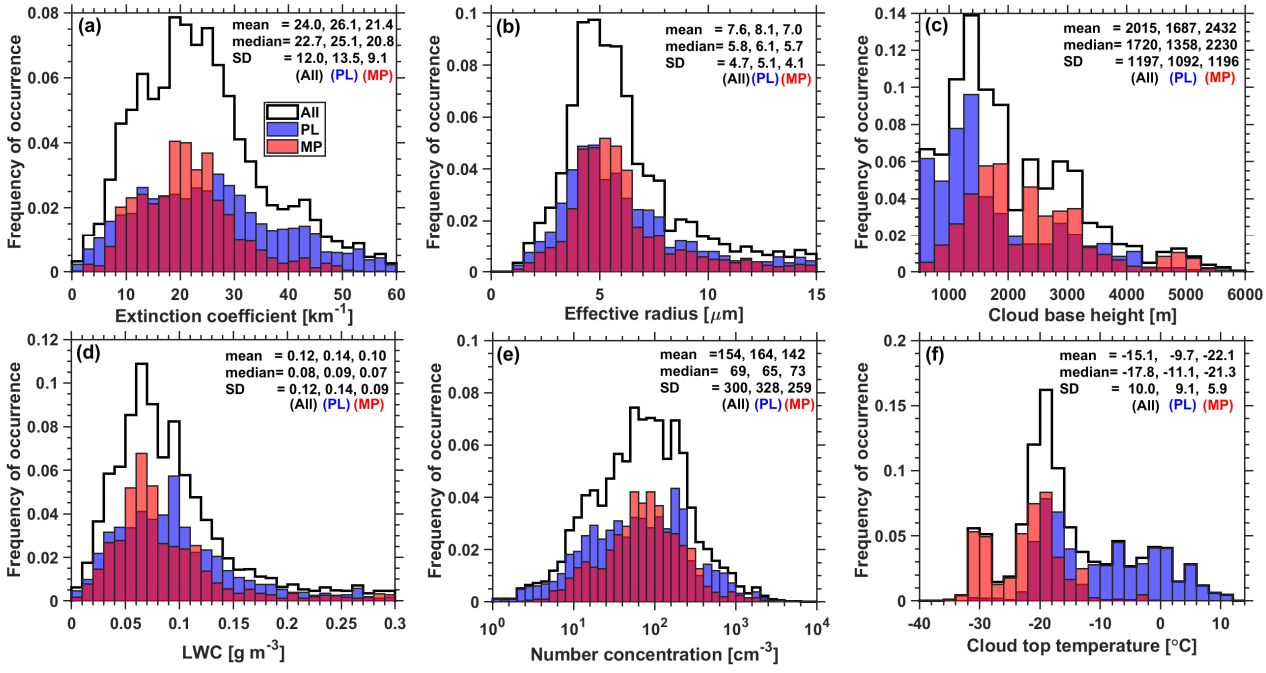

Figure 11. MOSAiC pure liquid (PL, blue) and mixed-phase (MP, red) clouds statistics. The statistics cover the liquid phase of clouds with base height >500 m in terms of (a) the droplet extinction coefficient, (b) effective droplet radius, (c) base height of the droplet-dominated cloud layer, (d) LWC, (e) CDNC, and (f) cloud top temperature. All available MOSAiC lidar observations of liquid-bearing cloud layers occuring at heights > 500 m are considered. The normalization (to 1.0) is applied to all clouds (PL+MP, in black). Median, mean, and SD values are given as numbers. The black histogram lines s are based on 3070 cloud data sets, the blue histograms (PL clouds) on 1721 data sets, and the red histograms (MP clouds) on 1349 data sets.

570 determined in the cloud base region at 75 m above cloud base height, are presented in panels a, b, d, and e. In panels c and f, the statistical distributions of cloud base heights (panel c) and estimated cloud top temperatures (panel f) are shown in addition. We distinguish between cloud events with ice virgae (MP, red histograms) and without ice virgae (PL, blue histograms). The black histogram lines consider all 3070 cloud profiles. The blue histograms provide insight into the cloud properties of stratiform Arctic clouds before significant ice nucleation sets in. The microphysical properties of the PL clouds as LWC and the droplet
575 extinction coefficient are strong functions of cloud temperature, which determines the amount of water vapor convertable into cloud liquid water. The cloud extinction coefficient also depends on the availability of CCNs. The red histograms show the characteristics of the liquid phase of mixed-phase clouds when all ice-formation-related processes (ice nucleation, ice crystal growths, riming, and droplet evaporation etc.), as described in the foregoing sections, influence the cloud properties in addition.

The histograms of the PL cloud properties in Fig. 11a, b,d, and e are slightly and partly even considerably broader than
580 the respective frequency-of-occurrence distributions for MPCs and shifted to larger values (see, e.g., panels a and d). This is related to the broader temperature distribution for PL clouds (see Fig. 11f) compared to the respective temperature histogram

https://doi.org/10.5194/egusphere-2025-967
Preprint. Discussion started: 17 March 2025

for MPCs and the shift of the PL-related temperature histogram towards higher temperatures. Note, that the temperature at cloud base, where CCN activation starts, is roughly 2-3 K higher than the temperature at cloud top (in panel f), where ice nucleation typically begins.

In Fig. 11a and b, the basic liquid-phase products, retrievable from the dual FOV lidar observations, are shown. The black curve, considering all clouds, shows a broad maximum of the extinction coefficient histogram with values from about 5 km^{-1} to about 45 km^{-1}. The PL extinction distribution is much broader than the respective MPC extinction distribution. In the case of ice-containing clouds, the number of clouds with high droplet extinction coefficients > 35 km^{-1} is significantly lower when compared to the respective numbers in the PL extinction histogram. The droplet extinction coefficients accumulated in the relatively narrow range from about 10-30 km^{-1}, probably the result of the WBF process, causing the evaporation of droplets, in combination with CCN activation and new droplet formation.

The PL- and MPC-related histograms are not very different in the case of the droplet effective radius. According to the black (PL+MP) histogram in Fig. 11b, a pronounced maximum from 3-7 μm is found. Most PL clouds and MPCs have LWCs between 0.03 and 0.13 g m^{-3} (Fig. 11d). However, there is a pronounced right wing in the distribution in the case of PL clouds, and even a shift of the MPC-related LWC distribution, compared to the PL-related distribution, towards smaller values. This distribution shift and the broad shape of the histogram reflect the impact of the cloud temperatures (see the distributions in Fig. 11f). A broad cloud temperature distribution is obtained with values from -22°C to $+12$°C in the case of PL cloud tops, whereas most cloud top temperatures are found between -16°C and -32°C in the case of MPCs. In the overlap region, the total amount (PL+MP) clouds shows a clear maximum around -20°C.

The CDNC histograms in Fig. 11e reflect the broad spectrum of CCN concentrations, i.e., aerosol conditions from very clean to heavy polluted Arctic haze and wildfire smoke situations. The CDNC histogram for pure liquid clouds spans over more than two orders of magnitude, from <10 cm^{-3} to about 1000 cm^{-3}. Again the CDNC distribution is more narrow when ice crystal nucleation and the WBF process (ice cyrstal growth) come into play. The overall (PL+MP) CDNC distribution shows a pronounced maximum from 10 to 500 cm^{-3}.

Zhang et al. (2019) presented year around lidar observations in Alaska (Utqiagvik, October 2013 to January 2017) and in Antarctica (Mc Murdo, December 2015 to January 2017). Their lidar-derived CDNC values were highest in winter (values accumulated in the range from 30-150 cm^{-3}) and lowest in the summer with most values between 15 to 40 cm^{-3} for the Arctic station. Zhang et al. (2019) also presented lidar estimates for the effective radius $R_{e,liq}$ in Arctic and Antarctic cloud layers. Most Arctic values were between 10 and 16 μm in summer and 4 and 9 μm in winter.

Figure 11c provides information about the heights at which the free tropospheric shallow clouds were typically observed (panel c). Most PL clouds layers are found below about 1800 to 2000 m height (with base heights below 1500 m). PL clouds with base heights above 1500 m up to 4200 m are less frequently observed. In contrast, most free tropospheric MPCs were detected at heights above 1000 m up to 3200 m. The highest clouds showing a liquid phase were observed above *Polarstern* at about 6.5 km height (as shown in Fig. 8 and 9). Silber and Shupe (2022) provide results of backward trajectory cluster analysis and air mass origin studies for all MOSAiC liquid-bearing cloud layers. Most of the air masses originated from the North Atlantic, Europe, and Asia, mostly from latitudes > 50°N.

https://doi.org/10.5194/egusphere-2025-967
Preprint. Discussion started: 17 March 2025

According to Griesche et al. (2021), our cloud statistics cover the so-called surface-decoupled fraction of Arctic stratiform clouds. These clouds develop in lofted aged aerosol layers reaching the Arctic after long-range transport from the surrounding continents and are not or only weakly influenced by local surface emissions. The main INP type in these lofted layers of complex aerosol mixtures is mineral dust (Carlsen and David, 2022). Biological particles and particles carrying biogenic or biological material also contribute to ice nucleation in the free troposphere during the short Arctic summer season from May to August (Carlsen and David, 2022). In the lowermost 500-600 m of the atmosphere (e.g., in the surface-coupled height regime) local particles with biogenic substances may dominate ice nucleation processes in the low-level clouds during the few summer months (Griesche et al., 2021; Creamean et al., 2022). The mineral dust fraction of Arctic haze controls heterogeneous ice nucleation even in the lowest part of the troposphere during the rest of the year (Creamean et al., 2022).

The cloud top temperature histograms in Fig. 11f indicate that a large fraction of the stratiform clouds (Pl + MP clouds) showed top temperatures from -18 to -22°C. A broad distribution with cloud top temperatures from $+12$°C down to -24°C was observed in the case of PL clouds. The MPC cloud top temperatures covered the range from -12°C to -34°C, with only a few exceptions towards higher temperatures.

The observations in Fig. 11c and f are in good agreement with respect to vertically resolved cloud height and cloud top temperature distributions, derived from multi-year spaceborne lidar and radar observations over the Arctic and presented by Carlsen and David (2022). A strong difference between winter (December to February) and summmer (June to August) conditions regarding heterogeneous ice nucleation was found. While in summer, significant ice nucleation started at -10 to -13°C, winter cloud top temperatures had to drop below about -17 to -24°C before ice nucleation sets. As mentioned, during the long winter season mineral dust particles prevail as INPs, while during the short summer period biological particles and particles carrying biogenic substances also contribute to ice nucleation.

6 MPC conceptual model: an update

The integration of the new dual FOV polarization technique into a state-of-the-art lidar-radar supersite enabled us to obtain a deeper insight into the evolution of Arctic MPCs. The improved monitoring of the ice phase together with the liquid phase, simultaneously and independently of each other, and this with high temporal resolution enabled us to study life cycles of MPC in large detail. This motivated us to update the conceptual model as it was presented by Morrison et al. (2012).

Briefly summarized, according to the conceptual model, a freshly formed opaque, shallow liquid-water cloud layer leads to strong longwave radiative cooling that initiates the formation of cluster-like updraft and downdraft fields of several kilometers (1-8 km). These larger scale turbulent structures develop even below the opaque cloud layer and influenced the air motion down to the surface, and thus can transport water vapor, CCN and INPs, after sublimation of ice crystals in the virgae, back into the cloud top layer. During updraft periods liquid and ice production preferably takes place (and respective heat release) and keeps the full MPC system alive as long as the synoptic scale humidity conditions allow for liquid water production. Similarly, droplet evaporation and ice crystal sublimation processes (and related cooling of the air) may strengthen the downdraft parts of the circulation pattern.

https://doi.org/10.5194/egusphere-2025-967
Preprint. Discussion started: 17 March 2025

Based on our MOSAiC lidar and radar observations we can add the following points to the conceptual model:

(1) CCN activation seems to play an important role throughout the lifetime of a MPC by permanently refilling the small-droplet fraction and stabilizing the droplet size distribution as a whole in this way. This could be concluded from the new dual FOV lidar observations.

(2) The MOSAiC polarization lidar observations confirm former studies (Ansmann et al., 2009; de Boer et al., 2011; Westbrook and Illingworth, 2011) that immersion freezing is the most relevant ice nucleation process in stratiform mixed phase clouds. A time-dependent ice nucleation mechanism paired with a large INP reservoir can sustain continuous ice crystal production for several hours as observed (Knopf et al., 2023).

(3) According to the one year MOSAiC aerosol observations, the CCN and INP reservoirs in the free troposphere were usually well filled. Recycling and entrainment of water vapor, CCNs and INPs from below and entrainment of CCN and INP from above seem to be responsible for refilling of the reservoirs. Precipitation can be regarded as the main sink of water vapor, CCNs and INPs.

(4) Only in a few cases, ice nucleation was found at temperatures > -15°C (in the free troposphere in the absence of any seeder-feeder impact). This may indicate the dominance of dust particles in ice nucleation processes in the free troposphere. Dust particles are active at temperatures around -20°C and lower. However, our lidar observations do not cover the lowermost height range with direct impact of local aerosols (nordic soil dust, biological material, biogenic substances). Low clouds layers occurr approximately 50% of the time and interact with the aerosol emitted in the Arctic..

(5) The perturbation of the main airflow (by orography and gravity waves) can sensitively influence the evolution of stratiform layered clouds even after hours or many kilometers downwind the perturbations. This is concluded from the discussion of the 21 September 2020 case study with the strong perturbation of the MPC evolution probably by gravity wave activity.

(6) The decreasing moisture content of an air mass, rather than empty CCN and INP reservoirs, is probably the reason for the dissolution of stratiform cloud layers in most cases.

7 Conclusion/Outlook

We presented the results of the one year MOSAiC observations of MPCs in the free troposphere with continuously running lidar and radar instrumentation aboard *Polarstern*, which drifted with pack ice close to the North Pole over many months. For the first time, the full winter half year from October to March was covered with aerosol and cloud observations in the North Pole region. We introduced the new dual FOV polarization lidar technique that allowed, for the first time, a robust and trustworthy monitoring of the liquid phase of stratiform MPC layers. In combination with the lidar-radar retrieval method, a detailed study of the life cycle of mixed phase clouds in terms of the liquid and ice phase microphysical properties was possible.

We presented two case studies of the life cycle of long-lived free tropospheric MPCs that corroborate the high potential of the new dual FOV lidar technique to characterize the optical and microphysical properties of the cloud droplets. The observations provided new insight into the interplay between the liquid and ice phase of Arctic MPCs. These observations demonstrate, that CCN activation is an important process to assure a longevity of an MPC deck. Also for the first time, we presented MPC

https://doi.org/10.5194/egusphere-2025-967
Preprint. Discussion started: 17 March 2025

statistical results in terms of geometrical, optical and microphysical properties for an entire year, covering all seasons of the year. The continuous lidar observation over the 360 MOSAiC days indicated that the aerosol concentration controls the number concentrations of ice crystals and droplets in Arctic stratiform clouds. The measurements further provided the impression that the CCN and INP reservoirs were always well filled, i.e., never depleted upon ice crystal formation.

As an outlook, we will continue with our MPC studies (life cycle studies, statistics as a function of aerosol pollution) by means of the new dual FOV technique implemented in lidar-radar supersites. Meanwhile we have long data sets from contrasting observations in Dushanbe, Tajikistan, Limassol, Cyprus, Punta Arenas in southern Chile (Radenz et al., 2021b), and Antarctica (Radenz et al., 2024). We plan long-term observations (2025-2026) in southern New Zealand. A first MPC lidar study was performed by Hofer et al. (2024). Overall goal is to characterize MPCs in a variety of different climate zones and at rather different environmental conditions to learn more about the aerosol impact to support MPC and climate-change modelling efforts.

8 Data availability

Polly lidar observations (level 0 data, measured signals) are in the PollyNet database (Polly, 2024). All the analysis products are available at TROPOS upon request (polly@tropos.de) and at https://doi.pangaea.de/10.1594/PANGAEA.935539 (Ohneiser et al., 2021). Cloud radar data are downloaded from the ARM data base (ARM, 2024; ARM-MOSAiC, 2024). MOSAiC radiosonde data are available at https://doi.org/10.1594/PANGAEA.928656 (Maturilli et al., 2021) Backward trajectory analysis has been performed by air mass transport computation with the NOAA (National Oceanic and Atmospheric Administration) HYSPLIT (HYbrid Single-Particle Lagrangian Integrated Trajectory) model (HYSPLIT, 2024).

9 Author contributions

The paper was written and designed by CJ and AA. The data analysis was performed by CJ, KO, MR, HB, JB, and HG. DAK, PS, and UW were involved in the interpretation of the findings. RE, HG, MR, JH, and DA took care of the lidar observations aboard *Polarstern* during MOSAiC. SD was responsible for high-quality MOSAiC *Polarstern* radiosonde launches. All coauthors were actively involved in the extended discussions and the elaboration of the final design of the manuscript

10 Competing interests

Daniel A. Knopf is a member of the editorial board of Atmospheric Chemistry and Physics

11 Financial support

The Multidisciplinary drifting Observatory for the Study of the Arctic Climate (MOSAiC) program was funded by the German Federal Ministry for Education and Research (BMBF) through financing the Alfred Wegener Institut Helmholtz Zentrum für

https://doi.org/10.5194/egusphere-2025-967
Preprint. Discussion started: 17 March 2025

Polar und Meeresforschung (AWI) and the *Polarstern* expedition PS122 under grant N-2014-H-060_Dethloff. The lidar analysis on smoke-cirrus interaction was further supported by BMBF funding of the SCiAMO project (MOSAIC-FKZ 03F0915A). The radiosonde program was funded by AWI awards AFMOSAiC-1_00 and AWI_PS122_00, the U.S. Department of Energy Atmospheric Radiation Measurement Program, and the German Weather Service. This project has also received funding from the European Union's Horizon 2020 research and innovation program ACTRIS-2 Integrating Activities (H2020-INFRAIA-2014 - 2015, grant agreement no. 654109) as well as from the European Union's Horizon Europe Programme under Grant Agreement No. 101137639 (CleanCloud). We gratefully acknowledge the funding by the Deutsche Forschungsgemeinschaft (DFG, German Research Foundation) – project no. 268020496 - TRR 172, within the Transregional Collaborative Research Center "ArctiC Amplification: Climate Relevant Atmospheric and SurfaCe Processes, and Feedback Mechanisms (AC)3". DAK acknowledges support by U.S. Department of Energy's (DOE) Atmospheric System Research (ASR) program, Office of Biological and Environmental Research (OBER) (grant no. DE-SC0021034).

Acknowledgements. Data used in this article were produced as part of the international Multidisciplinary drifting Observatory for the Study of the Arctic Climate (MOSAiC) with the tag MOSAiC20192020 and the Project_ID: AWI_PS122_00. We would like to thank everyone who contributed to the measurements used here (Nixdorf et al., 2021). Radiosonde data were obtained through a partnership between the leading Alfred Wegener Institute, the Atmospheric Radiation Measurement user facility, a U.S. Department of Energy facility managed by the Biological and Environmental Research Program, and the German Weather Service (DWD). We would like to thank the RV *Polarstern* crew for their perfect logistical support during the one-year MOSAiC expedition.

https://doi.org/10.5194/egusphere-2025-967
Preprint. Discussion started: 17 March 2025

References

Achtert, P., O'Connor, E. J., Brooks, I. M., Sotiropoulou, G., Shupe, M. D., Pospichal, B., Brooks, B. J., and Tjernström, M.: Properties of Arctic liquid and mixed-phase clouds from shipborne Cloudnet observations during ACSE 2014, Atmospheric Chemistry and Physics, 20, 14 983–15 002, https://doi.org/10.5194/acp-20-14983-2020, 2020.

Ansmann, A., Wandinger, U., Riebesell, M. A., Weitkamp, C., and Michaelis, W.: Independent measurement of extinction and backscatter profiles in cirrus clouds by using a combined Raman elastic-backscatter lidar, Appl. Opt., 31, 7113–7131, https://doi.org/10.1364/AO.31.007113, 1992.

Ansmann, A., Tesche, M., Althausen, D., Müller, D., Seifert, P., Freudenthaler, V., Heese, B., Wiegner, M., Pisani, G., Knippertz, P., and Dubovik, O.: Influence of Saharan dust on cloud glaciation in southern Morocco during the Saharan Mineral Dust Experiment, Journal of Geophysical Research: Atmospheres, 113, https://doi.org/10.1029/2007JD008785, 2008.

Ansmann, A., Tesche, M., Seifert, P., Althausen, D., Engelmann, R., Fruntke, J., Wandinger, U., Mattis, I., and Müller, D.: Evolution of the ice phase in tropical altocumulus: SAMUM lidar observations over Cape Verde, Journal of Geophysical Research: Atmospheres, 114, https://doi.org/10.1029/2008JD011659, 2009.

Ansmann, A., Petzold, A., Kandler, K., Tegen, I., Wendisch, M., Müller, D., Weinzierl, B., Müller, T., and Heintzenberg, J.: Saharan Mineral Dust Experiments SAMUM–1 and SAMUM–2: what have we learned?, Tellus B: Chemical and Physical Meteorology, https://doi.org/10.1111/j.1600-0889.2011.00555.x, 2011.

Ansmann, A., Mamouri, R.-E., Hofer, J., Baars, H., Althausen, D., and Abdullaev, S. F.: Dust mass, cloud condensation nuclei, and ice-nucleating particle profiling with polarization lidar: updated POLIPHON conversion factors from global AERONET analysis, Atmospheric Measurement Techniques, 12, 4849–4865, https://doi.org/10.5194/amt-12-4849-2019, 2019a.

Ansmann, A., Mamouri, R.-E., Bühl, J., Seifert, P., Engelmann, R., Hofer, J., Nisantzi, A., Atkinson, J. D., Kanji, Z. A., Sierau, B., Vrekoussis, M., and Sciare, J.: Ice-nucleating particle versus ice crystal number concentration in altocumulus and cirrus layers embedded in Saharan dust: a closure study, Atmospheric Chemistry and Physics, 19, 15 087–15 115, https://doi.org/10.5194/acp-19-15087-2019, 2019b.

Ansmann, A., Ohneiser, K., Mamouri, R.-E., Knopf, D. A., Veselovskii, I., Baars, H., Engelmann, R., Foth, A., Jimenez, C., Seifert, P., and Barja, B.: Tropospheric and stratospheric wildfire smoke profiling with lidar: mass, surface area, CCN, and INP retrieval, Atmospheric Chemistry and Physics, 21, https://doi.org/10.5194/acp-21-9779-2021, 2021.

Ansmann, A., Ohneiser, K., Chudnovsky, A., Knopf, D. A., Eloranta, E. W., Villanueva, D., Seifert, P., Radenz, M., Barja, B., Zamorano, F., Jimenez, C., Engelmann, R., Baars, H., Griesche, H., Hofer, J., Althausen, D., and Wandinger, U.: Ozone depletion in the Arctic and Antarctic stratosphere induced by wildfire smoke, Atmospheric Chemistry and Physics Discussions, 2022, 1–42, https://doi.org/10.5194/acp-2022-247, 2022.

Ansmann, A., Ohneiser, K., Engelmann, R., Radenz, M., Griesche, H., Hofer, J., Althausen, D., Creamean, J. M., Boyer, M. C., Knopf, D. A., Dahlke, S., Maturilli, M., Gebauer, H., Bühl, J., Jimenez, C., Seifert, P., and Wandinger, U.: Annual cycle of aerosol properties over the central Arctic during MOSAiC 2019–2020 – light-extinction, CCN, and INP levels from the boundary layer to the tropopause, Atmospheric Chemistry and Physics, 23, 12 821–12 849, https://doi.org/10.5194/acp-23-12821-2023, 2023.

Ansmann, A., Jimenez, C., Roschke, J., Bühl, J., Ohneiser, K., Engelmann, R., Radenz, M., Griesche, H., Hofer, J., Althausen, D., Knopf, D. A., Dahlke, S., Gaudek, T., Seifert, P., and Wandinger, U.: Impact of wildfire smoke on Arctic cirrus formation, part 1: analysis of MOSAiC 2019–2020 observations, EGUsphere, 2024, 1–29, https://doi.org/10.5194/egusphere-2024-2008, 2024a.

https://doi.org/10.5194/egusphere-2025-967
Preprint. Discussion started: 17 March 2025

Ansmann, A., Jimenez, C., Knopf, D. A., Roschke, J., Bühl, J., Ohneiser, K., and Engelmann, R.: Impact of wildfire smoke on Arctic cirrus formation, part 2: simulation of MOSAiC 2019–2020 cases, EGUsphere, 2024, 1–29, https://doi.org/10.5194/egusphere-2024-2009, 2024b.

ARM-MOSAiC(2024): Atmospheric Radiation Measurement (ARM) user facility, 2019, updated hourly, Ka ARM Zenith Radar (KAZR-CFRGE), 2019-10-11 to 2020-09-20, ARM Mobile Facility (MOS) MOSAIC (Drifting Obs - Study of Arctic Climate), AMF2 (M1), compiled by I. Lindenmaier, D. Nelson, B. Isom, J. Hardin, A. Matthews, T. Wendler, and V. Castro, ARM Data Center, last access: 13 December, 2024.

ARM(2024): Atmospheric Radiation Measurement mobile facility homepage, available at: https://www.arm.gov/data, last access: 29 November, 2024.

Baars, H., Kanitz, T., Engelmann, R., Althausen, D., Heese, B., Komppula, M., Preißler, J., Tesche, M., Ansmann, A., Wandinger, U., Lim, J.-H., Ahn, J. Y., Stachlewska, I. S., Amiridis, V., Marinou, E., Seifert, P., Hofer, J., Skupin, A., Schneider, F., Bohlmann, S., Foth, A., Bley, S., Pfüller, A., Giannakaki, E., Lihavainen, H., Viisanen, Y., Hooda, R. K., Pereira, S. N., Bortoli, D., Wagner, F., Mattis, I., Janicka, L., Markowicz, K. M., Achtert, P., Artaxo, P., Pauliquevis, T., Souza, R. A. F., Sharma, V. P., van Zyl, P. G., Beukes, J. P., Sun, J., Rohwer, E. G., Deng, R., Mamouri, R.-E., and Zamorano, F.: An overview of the first decade of Polly^{NET}: an emerging network of automated Raman-polarization lidars for.

Baars, H., Seifert, P., Engelmann, R., and Wandinger, U.: Target categorization of aerosol and clouds by continuous multiwavelength-polarization lidar measurements, Atmospheric Measurement Techniques, 10, 3175–3201, https://doi.org/10.5194/amt-10-3175-2017, 2017.

Bohlmann, S., Baars, H., Radenz, M., Engelmann, R., and Macke, A.: Ship-borne aerosol profiling with lidar over the Atlantic Ocean: from pure marine conditions to complex dust–smoke mixtures, Atmospheric Chemistry and Physics, 18, 9661–9679, https://doi.org/10.5194/acp-18-9661-2018, 2018.

Boucher, O., Randall, D., Artaxo, P., Bretherton, C., Feingold, G., Forster, P., Kerminen, V.-M., Kondo, Y., Liao, H., Lohmann, U., Rasch, P., Satheesh, S. K., S. S., Stevens, B., and Zhang, X. Y.: Clouds and aerosols, in *Climate Change 2013: The Physical Science Basis. Contribution of Working Group I to the Fifth Assessment Report of the Intergovernmental Panel on Climate Change*, T. F. Stocker, D. Qin, G.-K. Plattner, M. Tignor, S.K. Allen, J. Boschung, A. Nauels, Y. Xia, V. Bex and P.M. Midgley (Eds.), Cambridge University Press, Cambridge, United Kingdom and New York, NY, USA, pp. 571–657, https://www.ipcc.ch/site/assets/uploads/2018/02/WG1AR5_Chapter07_FINAL-1.pdf, 2013.

Boyer, M., Aliaga, D., Pernov, J. B., Angot, H., Quéléver, L. L. J., Dada, L., Heutte, B., Dall'Osto, M., Beddows, D. C. S., Brasseur, Z., Beck, I., Bucci, S., Duetsch, M., Stohl, A., Laurila, T., Asmi, E., Massling, A., Thomas, D. C., Nøjgaard, J. K., Chan, T., Sharma, S., Tunved, P., Krejci, R., Hansson, H. C., Bianchi, F., Lehtipalo, K., Wiedensohler, A., Weinhold, K., Kulmala, M., Petäjä, T., Sipilä, M., Schmale, J., and Jokinen, T.: A full year of aerosol size distribution data from the central Arctic under an extreme positive Arctic Oscillation: insights from the Multidisciplinary drifting Observatory for the Study of Arctic Climate (MOSAiC) expedition, Atmospheric Chemistry and Physics, 23, 389–415, https://doi.org/10.5194/acp-23-389-2023, 2023.

Bühl, J., Seifert, P., Myagkov, A., and Ansmann, A.: Measuring ice- and liquid-water properties in mixed-phase cloud layers at the Leipzig Cloudnet station, Atmospheric Chemistry and Physics, 16, 10 609–10 620, https://doi.org/10.5194/acp-16-10609-2016, 2016.

Bühl, J., Seifert, P., Radenz, M., Baars, H., and Ansmann, A.: Ice crystal number concentration from lidar, cloud radar and radar wind profiler measurements, Atmospheric Measurement Techniques, 12, 6601–6617, https://doi.org/10.5194/amt-12-6601-2019, 2019a.

https://doi.org/10.5194/egusphere-2025-967
Preprint. Discussion started: 17 March 2025

Bühl, J., Seifert, P., Engelmann, R., and Ansmann, A.: Impact of vertical air motions on ice formation rate in mixed-phase cloud layers, npj Climate and Atmospheric Science, 2, https://doi.org/10.1038/s41612-019-0092-6, 2019b.

Carlsen, T. and David, R. O.: Spaceborne Evidence That Ice-Nucleating Particles Influence High-Latitude Cloud Phase, Geophysical Research Letters, 49, e2022GL098 041, https://doi.org/10.1029/2022GL098041, e2022GL098041 2022GL098041, 2022.

Choudhury, G. and Tesche, M.: Estimating cloud condensation nuclei concentrations from CALIPSO lidar measurements, Atmospheric Measurement Techniques, 15, 639–654, https://doi.org/10.5194/amt-15-639-2022, 2022.

Choudhury, G., Ansmann, A., and Tesche, M.: Evaluation of aerosol number concentrations from CALIPSO with ATom airborne in situ measurements, Atmospheric Chemistry and Physics, 22, 7143–7161, https://doi.org/10.5194/acp-22-7143-2022, 2022.

Creamean, J., Barry, K., Hill, T., Hume, C., DeMott, P. J., Shupe, M. D., Dahlke, S., Willmes, S., Schmale, J., Beck, I., Hoppe, C. J. . M., Fong, A., Chamberlain, E., Bowman, J., Scharien, R., and Persson, O.: Annual cycle observations of aerosols capable of ice formation in central Arctic clouds, Nat. Commun., 13, https://doi.org/10.1038/s41467-022-31182-x, 2022.

Dai, G., Althausen, D., Hofer, J., Engelmann, R., Seifert, P., Bühl, J., Mamouri, R.-E., Wu, S., and Ansmann, A.: Calibration of Raman lidar water vapor profiles by means of AERONET photometer observations and GDAS meteorological data, Atmospheric Measurement Techniques, 11, 2735–2748, https://doi.org/10.5194/amt-11-2735-2018, 2018.

de Boer, G., Morrison, H., Shupe, M. D., and Hildner, R.: Evidence of liquid dependent ice nucleation in high-latitude stratiform clouds from surface remote sensors, Geophysical Research Letters, 38, https://doi.org/https://doi.org/10.1029/2010GL046016, 2011.

Delanoë, J. and Hogan, R. J.: A variational scheme for retrieving ice cloud properties from combined radar, lidar, and infrared radiometer, Journal of Geophysical Research: Atmospheres, 113, https://doi.org/10.1029/2007JD009000, 2008.

Donovan, D. P., Klein Baltink, H., Henzing, J. S., de Roode, S. R., and Siebesma, A. P.: A depolarisation lidar-based method for the determination of liquid-cloud microphysical properties, Atmospheric Measurement Techniques, 8, 237–266, https://doi.org/10.5194/amt-8-237-2015, 2015.

Eirund, G. K., Possner, A., and Lohmann, U.: Response of Arctic mixed-phase clouds to aerosol perturbations under different surface forcings, Atmospheric Chemistry and Physics, 19, 9847–9864, https://doi.org/10.5194/acp-19-9847-2019, 2019.

Engelmann, R., Kanitz, T., Baars, H., Heese, B., Althausen, D., Skupin, A., Wandinger, U., Komppula, M., Stachlewska, I. S., Amiridis, V., Marinou, E., Mattis, I., Linné, H., and Ansmann, A.: The automated multiwavelength Raman polarization and water-vapor lidar Polly^{XT}: the neXT generation, Atmospheric Measurement Techniques, 9, 1767–1784, https://doi.org/10.5194/amt-9-1767-2016, 2016.

Engelmann, R., Ansmann, A., Ohneiser, K., Griesche, H., Radenz, M., Hofer, J., Althausen, D., Dahlke, S., Maturilli, M., Veselovskii, I., Jimenez, C., Wiesen, R., Baars, H., Bühl, J., Gebauer, H., Haarig, M., Seifert, P., Wandinger, U., and Macke, A.: Wildfire smoke, Arctic haze, and aerosol effects on mixed-phase and cirrus clouds over the North Pole region during MOSAiC: an introduction, Atmospheric Chemistry and Physics, 21, https://doi.org/10.5194/acp-21-13397-2021, 2021.

Fridlind, A. M. and Ackerman, A. S.: Chapter 7 - Simulations of Arctic mixed-phase boundary layer clouds: Advances in understanding and outstanding questions, pp. 153–183, https://doi.org/https://doi.org/10.1016/B978-0-12-810549-8.00007-6, 2018.

Froyd, K. D., Yu, P., Schill, G. P., Brock, C. A., Kupc, A., Williamson, C. J., Jensen, E. J., Ray, E., Rosenlof, K. H., Bian, H., Darmenov, A. S., Colarco, P. R., Diskin, G. S., Bui, T., and Murphy, D. M.: Dominant role of mineral dust in cirrus cloud formation revealed by global-scale measurements, Nature Geoscience, 15, 177–183, https://doi.org/10.1038/s41561-022-00901-w, 2022.

Gong, X., Zhang, J., Croft, B., Yang, X., Frey, M. M., Bergner, N., Chang, R. Y.-W., Creamean, J. M., Kuang, C., Martin, R. V., Ranjithkumar, A., Sedlacek, A. J., Uin, J., Willmes, S., Zawadowicz, M. A., Pierce, J. R., Shupe, M. D., Schmale, J., and Wang, J.: Arctic warming by abundant fine sea salt aerosols from blowing snow, Nature Geoscience, 16, 768–774, https://doi.org/10.1038/s41561-023-01254-8, 2023.

https://doi.org/10.5194/egusphere-2025-967
Preprint. Discussion started: 17 March 2025

Grabowski, W. W.: Comparison of Eulerian Bin and Lagrangian Particle-Based Microphysics in Simulations of Nonprecipitating Cumulus, Journal of the Atmospheric Sciences, 77, 3951 – 3970, https://doi.org/10.1175/JAS-D-20-0100.1, 2020.

Griesche, H. J., Seifert, P., Ansmann, A., Baars, H., Barrientos Velasco, C., Bühl, J., Engelmann, R., Radenz, M., Zhenping, Y., and Macke, A.: Application of the shipborne remote sensing supersite OCEANET for profiling of Arctic aerosols and clouds during *Polarstern* cruise PS106, Atmospheric Measurement Techniques, 13, 5335–5358, https://doi.org/10.5194/amt-13-5335-2020, 2020.

Griesche, H. J., Ohneiser, K., Seifert, P., Radenz, M., Engelmann, R., and Ansmann, A.: Contrasting ice formation in Arctic clouds: surface-coupled vs. surface-decoupled clouds, Atmospheric Chemistry and Physics, 21, 10 357–10 374, https://doi.org/10.5194/acp-21-10357-2021, 2021.

Griesche, H. J., Barrientos-Velasco, C., Deneke, H., Hünerbein, A., Seifert, P., and Macke, A.: Low-level Arctic clouds: a blind zone in our knowledge of the radiation budget, Atmospheric Chemistry and Physics, 24, 597–612, https://doi.org/10.5194/acp-24-597-2024, 2024a.

Griesche, H. J., Seifert, P., Engelmann, R., Radenz, M., Hofer, J., Althausen, D., Walbröl, A., Barrientos-Velasco, C., Baars, H., Dahlke, S., Tukiainen, S., and Macke, A.: Cloud micro- and macrophysical properties from ground-based remote sensing during the MOSAiC drift experiment, Sci. Data, 11, https://doi.org/10.1038/s41597-024-03325-w, 2024b.

He, Y., Yin, Z., Ansmann, A., Liu, F., Wang, L., Jing, D., and Shen, H.: POLIPHON conversion factors for retrieving dust-related cloud condensation nuclei and ice-nucleating particle concentration profiles at oceanic sites, Atmospheric Measurement Techniques, 16, 1951–1970, https://doi.org/10.5194/amt-16-1951-2023, 2023.

Heutte, B., Bergner, N., Angot, H., Pernov, J. B., Dada, L., Mirrielees, J. A., Beck, I., Baccarini, A., Boyer, M., Creamean, J. M., Daellenbach, K. R., El Haddad, I., Frey, M. M., Henning, S., Laurila, T., Moschos, V., Petäjä, T., Pratt, K. A., Quéléver, L. L. J., Shupe, M. D., Zieger, P., Jokinen, T., and Schmale, J.: Observations of high time-resolution and size-resolved aerosol chemical composition and microphyscis in the central Arctic: implications for climate-relevant particle properties, EGUsphere, 2024, 1–64, https://doi.org/10.5194/egusphere-2024-1912, 2024.

Hobbs, P. V. and Rangno, A. L.: Ice Particle Concentrations in Clouds, Journal of Atmospheric Sciences, 42, 2523 – 2549, https://doi.org/10.1175/1520-0469(1985)042<2523:IPCIC>2.0.CO;2, 1985.

Hofer, J., Althausen, D., Abdullaev, S. F., Makhmudov, A. N., Nazarov, B. I., Schettler, G., Engelmann, R., Baars, H., Fomba, K. W., Müller, K., Heinold, B., Kandler, K., and Ansmann, A.: Long-term profiling of mineral dust and pollution aerosol with multiwavelength polarization Raman lidar at the Central Asian site of Dushanbe, Tajikistan: case studies, Atmospheric Chemistry and Physics, 17, 14 559–14 577, https://doi.org/10.5194/acp-17-14559-2017, 2017.

Hofer, J., Seifert, P., Liley, J. B., Radenz, M., Uchino, O., Morino, I., Sakai, T., Nagai, T., and Ansmann, A.: Aerosol-related effects on the occurrence of heterogeneous ice formation over Lauder, New Zealand / Aotearoa, Atmospheric Chemistry and Physics, 24, 1265–1280, https://doi.org/10.5194/acp-24-1265-2024, 2024.

HYSPLIT(2024): HYbrid Single-Particle Lagrangian Integrated Trajectory model, backward trajectory calculation tool, available at: http://ready.arl.noaa.gov/HYSPLIT_traj.php, last access: 20 November, 2024.

Illingworth, A. J., Hogan, R. J., O'Connor, E., Bouniol, D., Brooks, M. E., Delanoé, J., Donovan, D. P., Eastment, J. D., Gaussiat, N., Goddard, J. W. F., Haeffelin, M., Baltink, H. K., Krasnov, O. A., Pelon, J., Piriou, J.-M., Protat, A., Russchenberg, H. W. J., Seifert, A., Tompkins, A. M., van Zadelhoff, G.-J., Vinit, F., Willén, U., Wilson, D. R., and Wrench, C. L.: Cloudnet: Continuous Evaluation of Cloud Profiles in Seven Operational Models Using Ground-Based Observations, Bulletin of the American Meteorological Society, 88, 883 – 898, https://doi.org/10.1175/BAMS-88-6-883, 2007.

https://doi.org/10.5194/egusphere-2025-967
Preprint. Discussion started: 17 March 2025

Jimenez, C.: Observations of aerosol and liquid-water clouds with Dual-Field-of-View Polarization Lidar – A ground-based view on aerosol-cloud interactions, University of Leipzig, Germany, 182p, https://nbn-resolving.org/urn:nbn:de:bsz:15-qucosa2-769056, 2021.

Jimenez, C., Ansmann, A., Engelmann, R., Donovan, D., Malinka, A., Schmidt, J., Seifert, P., and Wandinger, U.: The dual-field-of-view polarization lidar technique: a new concept in monitoring aerosol effects in liquid-water clouds – theoretical framework, Atmospheric Chemistry and Physics, 20, 15 247–15 263, https://doi.org/10.5194/acp-20-15247-2020, 2020a.

Jimenez, C., Ansmann, A., Engelmann, R., Donovan, D., Malinka, A., Seifert, P., Wiesen, R., Radenz, M., Yin, Z., Bühl, J., Schmidt, J., Barja, B., and Wandinger, U.: The dual-field-of-view polarization lidar technique: a new concept in monitoring aerosol effects in liquid-water clouds – case studies, Atmospheric Chemistry and Physics, 20, 15 265–15 284, https://doi.org/10.5194/acp-20-15265-2020, 2020b.

Kalesse, H., de Boer, G., Solomon, A., Oue, M., Ahlgrimm, M., Zhang, D., Shupe, M. D., Luke, E., and Protat, A.: Understanding Rapid Changes in Phase Partitioning between Cloud Liquid and Ice in Stratiform Mixed-Phase Clouds: An Arctic Case Study, Monthly Weather Review, 144, 4805 – 4826, https://doi.org/10.1175/MWR-D-16-0155.1, 2016.

Kanitz, T., Seifert, P., Ansmann, A., Engelmann, R., Althausen, D., Casiccia, C., and Rohwer, E. G.: Contrasting the impact of aerosols at northern and southern midlatitudes on heterogeneous ice formation, Geophys. Res. Lett., 38, https://doi.org/10.1029/2011GL048532, 2011.

Khain, A., Pinsky, M., and Korolev, A.: Combined Effect of the Wegener–Bergeron–Findeisen Mechanism and Large Eddies on Microphysics of Mixed-Phase Stratiform Clouds, Journal of the Atmospheric Sciences, 79, 383 – 407, https://doi.org/10.1175/JAS-D-20-0269.1, 2022.

Knopf, D. A., Silber, I., Riemer, N., Fridlind, A. M., and Ackerman, A. S.: A 1D Model for Nucleation of Ice From Aerosol Particles: An Application to a Mixed-Phase Arctic Stratus Cloud Layer, Journal of Advances in Modeling Earth Systems, 15, e2023MS003 663, https://doi.org/10.1029/2023MS003663, e2023MS003663 2023MS003663, 2023.

Knust, R.: Polar Research and Supply Vessel POLARSTERN operated by the Alfred-Wegener-Institute, Journal of large-scale research facilities JLSRF, 3, A119, https://doi.org/10.17815/jlsrf-3-163, 2017.

Korolev, A.: Limitations of the Wegener–Bergeron–Findeisen Mechanism in the Evolution of Mixed-Phase Clouds, Journal of the Atmospheric Sciences, 64, 3372 – 3375, https://doi.org/10.1175/JAS4035.1, 2007.

Korolev, A. and Field, P. R.: The Effect of Dynamics on Mixed-Phase Clouds: Theoretical Considerations, Journal of the Atmospheric Sciences, 65, 66 – 86, https://doi.org/10.1175/2007JAS2355.1, 2008.

Korolev, A., McFarquhar, G., Field, P. R., Franklin, C., Lawson, P., Wang, Z., Williams, E., Abel, S. J., Axisa, D., Borrmann, S., Crosier, J., Fugal, J., Krämer, M., Lohmann, U., Schlenczek, O., Schnaiter, M., and Wendisch, M.: Mixed-Phase Clouds: Progress and Challenges, Meteorological Monographs, 58, 5.1 – 5.50, https://doi.org/10.1175/AMSMONOGRAPHS-D-17-0001.1, 2017.

Lohmann, U. and Neubauer, D.: The importance of mixed-phase and ice clouds for climate sensitivity in the global aerosol–climate model ECHAM6-HAM2, Atmospheric Chemistry and Physics, 18, 8807–8828, https://doi.org/10.5194/acp-18-8807-2018, 2018.

Mamouri, R.-E. and Ansmann, A.: Potential of polarization lidar to provide profiles of CCN- and INP-relevant aerosol parameters, Atmospheric Chemistry and Physics, 16, 5905–5931, https://doi.org/10.5194/acp-16-5905-2016, 2016.

Mamouri, R.-E. and Ansmann, A.: Potential of polarization/Raman lidar to separate fine dust, coarse dust, maritime, and anthropogenic aerosol profiles, Atmospheric Measurement Techniques, 10, 3403–3427, https://doi.org/10.5194/amt-10-3403-2017, 2017.

Marinou, E., Tesche, M., Nenes, A., Ansmann, A., Schrod, J., Mamali, D., Tsekeri, A., Pikridas, M., Baars, H., Engelmann, R., Voudouri, K.-A., Solomos, S., Sciare, J., Groß, S., Ewald, F., and Amiridis, V.: Retrieval of ice-nucleating particle concentrations from lidar observations and comparison with UAV in situ measurements, Atmospheric Chemistry and Physics, 19, 11 315–11 342, https://doi.org/10.5194/acp-19-11315-2019, 2019.

https://doi.org/10.5194/egusphere-2025-967
Preprint. Discussion started: 17 March 2025

Mason, S. L., Hogan, R. J., Bozzo, A., and Pounder, N. L.: A unified synergistic retrieval of clouds, aerosols, and precipitation from EarthCARE: the ACM-CAP product, Atmospheric Measurement Techniques, 16, 3459–3486, https://doi.org/10.5194/amt-16-3459-2023, 2023.

Maturilli, M., Holdridge, D. J., Dahlke, S., Graeser, J., Sommerfeld, A., Jaiser, R., Deckelmann, H., and Schulz, A.: Initial radiosonde data from 2019-10 to 2020-09 during project MOSAiC, https://doi.org/10.1594/PANGAEA.928656, 2021.

Mioche, G., Jourdan, O., Delanoë, J., Gourbeyre, C., Febvre, G., Dupuy, R., Monier, M., Szczap, F., Schwarzenboeck, A., and Gayet, J.-F.: Vertical distribution of microphysical properties of Arctic springtime low-level mixed-phase clouds over the Greenland and Norwegian seas, Atmospheric Chemistry and Physics, 17, 12 845–12 869, https://doi.org/10.5194/acp-17-12845-2017, 2017.

Morrison, H., Zuidema, P., Ackerman, A. S., Avramov, A., de Boer, G., Fan, J., Fridlind, A. M., Hashino, T., Harrington, J. Y., Luo, Y., Ovchinnikov, M., and Shipway, B.: Intercomparison of cloud model simulations of Arctic mixed-phase boundary layer clouds observed during SHEBA/FIRE-ACE, Journal of Advances in Modeling Earth Systems, 3, M06 003, https://doi.org/10.1029/2011MS000066, 2011.

Morrison, H., De Boer, G., Feingold, G., Harrington, J., Shupe, M. D., and Sulia, K.: Resilience of persistent Arctic mixed-phase clouds, Nature Geoscience, 5, 11–17, https://doi.org/10.1038/ngeo1332, 2012.

Morrison, H., van Lier-Walqui, M., Fridlind, A. M., Grabowski, W. W., Harrington, J. Y., Hoose, C., Korolev, A., Kumjian, M. R., Milbrandt, J. A., Pawlowska, H., Posselt, D. J., Prat, O. P., Reimel, K. J., Shima, S.-I., van Diedenhoven, B., and Xue, L.: Confronting the Challenge of Modeling Cloud and Precipitation Microphysics, Journal of Advances in Modeling Earth Systems, 12, e2019MS001 689, https://doi.org/10.1029/2019MS001689, e2019MS001689 2019MS001689, 2020.

Nixdorf, U., Dethloff, K., Rex, M., Shupe, M., Sommerfeld, A., Perovich, D., Nicolaus, M., Heuze´, C., Rabe, B., Loose, B., Damm, E., Gradinger, R., Fong., A, Maslowski, W., Rinke, A., Kwok, R., Spreen, G., Wendisch, M., Herber, A., Hirsekorn, M., Mohaupt, V., Frickenhaus, S., Immerz, A., Weiss-Tuider, K., König, B., Mengedoht, D., Regnery, J., Gerchow, P., Ransby, D., Krumpen, T., Morgenstern, A., Haas, C., Kanzow, T., Rack, F. R., Saitzev, V., Sokolov, V., Makarov, A., Schwarze, S., Wunderlich, T., Wurr, K., and Boetius, A.: MOSAiC extended acknowledgement, Zenodo, https://doi.org/10.5281/zenodo.5179738, 2021.

Ohneiser, K., Ansmann, A., Baars, H., Seifert, P., Barja, B., Jimenez, C., Radenz, M., Teisseire, A., Floutsi, A., Haarig, M., Foth, A., Chudnovsky, A., Engelmann, R., Zamorano, F., Bühl, J., and Wandinger, U.: Smoke of extreme Australian bushfires observed in the stratosphere over Punta Arenas, Chile, in January 2020: optical thickness, lidar ratios, and depolarization ratios at 355 and 532 nm, Atmospheric Chemistry and Physics, 20, 8003–8015, https://doi.org/10.5194/acp-20-8003-2020, 2020.

Ohneiser, K., Ansmann, A., Chudnovsky, A., Engelmann, R., Ritter, C., Veselovskii, I., Baars, H., Gebauer, H., Griesche, H., Radenz, M., Hofer, J., Althausen, D., Dahlke, S., and Maturilli, M.: The unexpected smoke layer in the High Arctic winter stratosphere during MOSAiC 2019–2020, Atmospheric Chemistry and Physics, 21, 15 783–15 808, https://doi.org/10.5194/acp-21-15783-2021, 2021.

Ohneiser, K., Ansmann, A., Kaifler, B., Chudnovsky, A., Barja, B., Knopf, D. A., Kaifler, N., Baars, H., Seifert, P., Villanueva, D., Jimenez, C., Radenz, M., Engelmann, R., Veselovskii, I., and Zamorano, F.: Australian wildfire smoke in the stratosphere: the decay phase in 2020/21 and impact on ozone depletion, Atmospheric Chemistry and Physics Discussions, 2022, 1–41, https://doi.org/10.5194/acp-2021-1097, 2022.

Ohneiser, K., Ansmann, A., Witthuhn, J., Deneke, H., Chudnovsky, A., Walter, G., and Senf, F.: Self-lofting of wildfire smoke in the troposphere and stratosphere: simulations and space lidar observations, Atmospheric Chemistry and Physics, 23, 2901–2925, https://doi.org/10.5194/acp-23-2901-2023, 2023.

Polly(2024): PollyNET lidar data base, available at: http://polly.tropos.de/, last access: 10 December, 2024.

https://doi.org/10.5194/egusphere-2025-967
Preprint. Discussion started: 17 March 2025

Radenz, M., Seifert, P., Baars, H., Floutsi, A. A., Yin, Z., and Bühl, J.: Automated time–height-resolved air mass source attribution for profiling remote sensing applications, Atmospheric Chemistry and Physics, 21, 3015–3033, https://doi.org/10.5194/acp-21-3015-2021, 2021a.

Radenz, M., Bühl, J., Seifert, P., Baars, H., Engelmann, R., Barja González, B., Mamouri, R.-E., Zamorano, F., and Ansmann, A.: Hemispheric contrasts in ice formation in stratiform mixed-phase clouds: disentangling the role of aerosol and dynamics with ground-based remote sensing, Atmospheric Chemistry and Physics, 21, 17 969–17 994, https://doi.org/10.5194/acp-21-17969-2021, 2021b.

Radenz, M., Engelmann, R., Henning, S., Schmithüsen, H., Baars, H., Frey, M. M., Weller, R., Bühl, J., Jimenez, C., Roschke, J., Muser, L. O., Wullenweber, N., Zeppenfeld, S., Griesche, H., Wandinger, U., and Seifert, P.: Ground-Based Remote Sensing of Aerosol, Clouds, Dynamics, and Precipitation in Antarctica: First Results from the 1-Year COALA Campaign at Neumayer Station III in 2023, Bulletin of the American Meteorological Society, 105, E1438 – E1457, https://doi.org/10.1175/BAMS-D-22-0285.1, 2024.

Ramelli, F., Henneberger, J., David, R. O., Bühl, J., Radenz, M., Seifert, P., Wieder, J., Lauber, A., Pasquier, J. T., Engelmann, R., Mignani, C., Hervo, M., and Lohmann, U.: Microphysical investigation of the seeder and feeder region of an Alpine mixed-phase cloud, Atmospheric Chemistry and Physics, 21, 6681–6706, https://doi.org/10.5194/acp-21-6681-2021, 2021.

Rauber, R. M. and Tokay, A.: An Explanation for the Existence of Supercooled Water at the Top of Cold Clouds, Journal of Atmospheric Sciences, 48, 1005 – 1023, https://doi.org/10.1175/1520-0469(1991)048<1005:AEFTEO>2.0.CO;2, 1991.

Roesler, E. L., Posselt, D. J., and Rood, R. B.: Using large eddy simulations to reveal the size, strength, and phase of updraft and downdraft cores of an Arctic mixed-phase stratocumulus cloud, Journal of Geophysical Research: Atmospheres, 122, 4378–4400, https://doi.org/10.1002/2016JD026055, 2017.

Rose, T., Crewell, S., Löhnert, U., and Simmer, C.: A network suitable microwave radiometer for operational monitoring of the cloudy atmosphere, Atmos. Res., 75, 183–200, https://doi.org/10.1016/j.atmosres.2004.12.005, 2005.

Savre, J. and Ekman, A. M. L.: Large-eddy simulation of three mixed-phase cloud events during ISDAC: Conditions for persistent heterogeneous ice formation, Journal of Geophysical Research: Atmospheres, 120, 7699–7725, https://doi.org/10.1002/2014JD023006, 2015.

Schmidt, J., Wandinger, U., and Malinka, A.: Dual-field-of-view Raman lidar measurements for the retrieval of cloud microphysical properties, Appl. Opt., 52, 2235–2247, https://doi.org/10.1364/AO.52.002235, 2013.

Schmidt, J., Ansmann, A., Bühl, J., Baars, H., Wandinger, U., Müller, D., and Malinka, A. V.: Dual-FOV Raman and Doppler lidar studies of aerosol-cloud interactions: Simultaneous profiling of aerosols, warm-cloud properties, and vertical wind, Journal of Geophysical Research: Atmospheres, 119, 5512–5527, https://doi.org/10.1002/2013JD020424, 2014.

Schmidt, J., Ansmann, A., Bühl, J., and Wandinger, U.: Strong aerosol–cloud interaction in altocumulus during updraft periods: lidar observations over central Europe, Atmospheric Chemistry and Physics, 15, 10 687–10 700, https://doi.org/10.5194/acp-15-10687-2015, 2015.

Seidel, C., Althausen, D., Ansmann, A., Wendisch, M., Griesche, H. J., Radenz, M., Hofer, J., Dahlke, S., Maturilli, M., Wahlbrol, A., Baars, H., and Engelmann, R.: Close correlation between vertically integrated tropospheric water vapor and the downward, broadband thermal-infrared irradiance at the ground: Observations in the Central Arctic during MOSAiC, Journal of Geophysical Research: Atmospheres, p. submitted, https://doi.org/10.1029/2024JD042378, 2024.

Shupe, M. D.: A ground-based multisensor cloud phase classifier, Geophysical Research Letters, 34, https://doi.org/10.1029/2007GL031008, 2007.

Shupe, M. D., Matrosov, S. Y., and Uttal, T.: Arctic Mixed-Phase Cloud Properties Derived from Surface-Based Sensors at SHEBA, Journal of the Atmospheric Sciences, 63, 697 – 711, https://doi.org/10.1175/JAS3659.1, 2006.

https://doi.org/10.5194/egusphere-2025-967
Preprint. Discussion started: 17 March 2025

Shupe, M. D., Kollias, P., Persson, P. O. G., and McFarquhar, G. M.: Vertical Motions in Arctic Mixed-Phase Stratiform Clouds, Journal of the Atmospheric Sciences, 65, 1304 – 1322, https://doi.org/10.1175/2007JAS2479.1, 2008.

Shupe, M. D., Rex, M., Blomquist, B., Ola, P., Persson, G., Schmale, J., Uttal, T., Althausen, D., Angot, H., Archer, S., Bariteau, L., Beck, I., Bilberry, J., Bucci, S., Buck, C., Boyer, M., Brasseur, Z., Brooks, I. M., Calmer, R., Cassano, J., Castro, V., Chu, D., Costa, D., Cox, C. J., Creamean, J., Crewell, S., Dahlke, S., Damm, E., de Boer, G., Deckelmann, H., Dethloff, K., Dütsch, M., Ebell, K., Ehrlich, A., Ellis, J., Engelmann, R., Fong, A. A., Frey, M. M., Gallagher, M. R., Ganzeveld, L., Gradinger, R., Graeser, J., Greenamyer, V., Griesche, H., Griffiths, S., Hamilton, J., Heinemann, G., Helmig, D., Herber, A., Heuzé, C., Hofer, J., Houchens, T., Howard, D., Inoue, J., Jacobi, H.-W., Jaiser, R., Jokinen, T., Jourdan, O., Jozef, G., King, W., Kirchgaessner, A., Klingebiel, M., Krassovski, M., Krumpen, T., Lampert, A., Landing, W., Laurila, T., Lawrence, D., Lonardi, M., Loose, B., Lüpkes, C., Maahn, M., Macke, A., Maslowski, W., Marsay, C., Maturilli, M., Mech, M., Morris, S., Moser, M., Nicolaus, M., Ortega, P., Osborn, J., Pätzold, F., Perovich, D. K., Petäjä, T., Pilz, C., Pirazzini, R., Posman, K., Powers, H., Pratt, K. A., Preußer, A., Quéléver, L., Radenz, M., Rabe, B., Rinke, A., Sachs, T., Schulz, A., Siebert, H., Silva, T., Solomon, A., Sommerfeld, A., Spreen, G., Stephens, M., Stohl, A., Svensson, G., Uin, J., Viegas, J., Voigt, C., von der Gathen, P., Wehner, B., Welker, J. M., Wendisch, M., Werner, M., Xie, Z., and Yue, F.: Overview of the MOSAiC expedition: Atmosphere, Elementa: Science of the Anthropocene, 10, https://doi.org/10.1525/elementa.2021.00060, 2022.

Silber, I. and Shupe, M. D.: Insights on sources and formation mechanisms of liquid-bearing clouds over MOSAiC examined from a Lagrangian framework, Elementa: Science of the Anthropocene, 10, 000 071, https://doi.org/10.1525/elementa.2021.000071, 2022.

Snider, J. R., Leon, D., and Wang, Z.: Droplet Concentration and Spectral Broadening in Southeast Pacific Stratocumulus Clouds, Journal of the Atmospheric Sciences, 74, 719 – 749, https://doi.org/10.1175/JAS-D-16-0043.1, 2017.

Solomon, A., de Boer, G., Creamean, J. M., McComiskey, A., Shupe, M. D., Maahn, M., and Cox, C.: The relative impact of cloud condensation nuclei and ice nucleating particle concentrations on phase partitioning in Arctic mixed-phase stratocumulus clouds, Atmospheric Chemistry and Physics, 18, 17 047–17 059, https://doi.org/10.5194/acp-18-17047-2018, 2018.

Sourdeval, O., Gryspeerdt, E., Krämer, M., Goren, T., Delanoë, J., Afchine, A., Hemmer, F., and Quaas, J.: Ice crystal number concentration estimates from lidar–radar satellite remote sensing – Part 1: Method and evaluation, Atmospheric Chemistry and Physics, 18, 14 327–14 350, https://doi.org/10.5194/acp-18-14327-2018, 2018.

Vali, G. and Snider, J. R.: Time-dependent freezing rate parcel model, Atmospheric Chemistry and Physics, 15, 2071–2079, https://doi.org/10.5194/acp-15-2071-2015, 2015.

Waitz, F., Schnaiter, M., Leisner, T., and Järvinen, E.: In situ observation of riming in mixed-phase clouds using the PHIPS probe, Atmospheric Chemistry and Physics, 22, 7087–7103, https://doi.org/10.5194/acp-22-7087-2022, 2022.

Wendisch, M., Macke, A., Ehrlich, A., Lüpkes, C., Mech, M., Chechin, D., Dethloff, K., Velasco, C. B., Bozem, H., Brückner, M., Clemen, H.-C., Crewell, S., Donth, T., Dupuy, R., Ebell, K., Egerer, U., Engelmann, R., Engler, C., Eppers, O., Gehrmann, M., Gong, X., Gottschalk, M., Gourbeyre, C., Griesche, H., Hartmann, J., Hartmann, M., Heinold, B., Herber, A., Herrmann, H., Heygster, G., Hoor, P., Jafariserajehlou, S., Jäkel, E., Järvinen, E., Jourdan, O., Kästner, U., Kecorius, S., Knudsen, E. M., Köllner, F., Kretzschmar, J., Lelli, L., Leroy, D., Maturilli, M., Mei, L., Mertes, S., Mioche, G., Neuber, R., Nicolaus, M., Nomokonova, T., Notholt, J., Palm, M., van Pinxteren, M., Quaas, J., Richter, P., Ruiz-Donoso, E., Schäfer, M., Schmieder, K., Schnaiter, M., Schneider, J., Schwarzenböck, A., Seifert, P., Shupe, M. D., Siebert, H., Spreen, G., Stapf, J., Stratmann, F., Vogl, T., Welti, A., Wex, H., Wiedensohler, A., Zanatta, M., and Zeppenfeld, S.: The Arctic Cloud Puzzle: Using ACLOUD/PASCAL Multiplatform Observations to Unravel the Role of Clouds and Aerosol Particles in Arctic Amplification, Bulletin of the American Meteorological Society, 100, 841 – 871, https://doi.org/10.1175/BAMS-D-18-0072.1, 2019.

https://doi.org/10.5194/egusphere-2025-967
Preprint. Discussion started: 17 March 2025

Westbrook, C. D. and Illingworth, A. J.: Evidence that ice forms primarily in supercooled liquid clouds at temperatures > -27°C, Geophysical Research Letters, 38, https://doi.org/10.1029/2011GL048021, 2011.

Worldview-earthdata-nasa-2024: Satellite images, available at: https://worldview.earthdata.nasa.gov/?v=-735094.46733622,-135866.03606716794,670935.2615954294,740494.9593628328&p=arctic&l=Reference_Labels_15m(hidden),Reference_Features_15m(hidden),Coastlines_15m,VIIRS_NOAA20_Brightness_Temp_BandI5_Night(hidden),VIIRS_SNPP_Brightness_Temp_BandI5_Night(min=218.9,max=259.6,squash=true),VIIRS_NOAA21_CorrectedReflectance_TrueColor(hidden),VIIRS_NOAA20_CorrectedReflectance_TrueColor(hidden),VIIRS_SNPP_CorrectedReflectance_TrueColor,MODIS_Aqua_CorrectedReflectance_TrueColor(hidden),MODIS_Terra_CorrectedReflectance_TrueColor(hidden)&lg=true&s=116.1592,86.6208&t=2019-12-30-T08%3A58%3A25Z, last access: 10 December, 2024.

Yin, Z., Ansmann, A., Baars, H., Seifert, P., Engelmann, R., Radenz, M., Jimenez, C., Herzog, A., Ohneiser, K., Hanbuch, K., Blarel, L., Goloub, P., Dubois, G., Victori, S., and Maupin, F.: Aerosol measurements with a shipborne Sun–sky–lunar photometer and collocated multiwavelength Raman polarization lidar over the Atlantic Ocean, Atmospheric Measurement Techniques, 12, 5685–5698, https://doi.org/10.5194/amt-12-5685-2019, 2019.

Zhang, D., Vogelmann, A., Kollias, P., Luke, E., Yang, F., Lubin, D., and Wang, Z.: Comparison of Antarctic and Arctic Single-Layer Stratiform Mixed-Phase Cloud Properties Using Ground-Based Remote Sensing Measurements, Journal of Geophysical Research: Atmospheres, 124, 10 186–10 204, https://doi.org/https://doi.org/10.1029/2019JD030673, 2019.